Unraveling Pathways of Elevated Ozone Induced by the 2020 Lockdown in Europe by an Observationally Constrained Regional Model using TROPOMI

Amir H. Souri[1*], Kelly Chance[1], Juseon Bak[2], Caroline R. Nowlan[1], Gonzalo González Abad[1],

Yeonjin Jung[1], David C. Wong[3], Jingqiu Mao[4,5], and Xiong Liu[1]

[1]Atomic and Molecular Physics (AMP) Division, Harvard–Smithsonian Center for Astrophysics, Cambridge, MA,

USA

[2]Institute of Environmental Studies, Pusan National University, Busan, South Korea

[3]U.S. Environmental Protection Agency, Center for Environmental Measurement & Modeling, Research Triangle

Park, NC, USA

[4]Geophysical Institute, University of Alaska Fairbanks, Fairbanks, AK, USA

[5]Department of Chemistry and Biochemistry, University of Alaska Fairbanks, Fairbanks, AK, USA

* Corresponding author: ahsouri@cfa.harvard.edu

Abstract. Questions about how emissions are changing during the COVID-19 lockdown periods cannot be answered by observations of atmospheric trace gas concentrations alone, in part due to simultaneous changes in atmospheric transport, emissions, dynamics, photochemistry, and chemical feedback. A chemical transport model simulation benefiting from a multi-species inversion framework using well-characterized observations should differentiate those influences enabling to closely examine changes in emissions. Accordingly, we jointly constrain NO_x and VOC emissions using well-characterized TROPOMI HCHO and NO_2 columns during the months of March, April, and May 2020 (lockdown) and 2019 (baseline). We observe a noticeable decline in the magnitude of NO_x emissions in March 2020 (14-31%) in several major cities including Paris, London, Madrid, and Milan expanding further to Rome, Brussels, Frankfurt, Warsaw, Belgrade, Kyiv, and Moscow (34-51%) in April. However, NO_x emissions remain at somewhat similar values or even higher in some portions of the UK, Poland, and Moscow in March 2020 compared to the baseline possibly due to the timeline of restrictions. Comparisons against surface monitoring stations indicate that the constrained model underrepresents the reduction in surface NO_2. This underrepresentation correlates with the TROPOMI frequency impacted by cloudiness. During the month of April, when ample TROPOMI samples are present, the surface NO_2 reductions occurring in polluted areas are described fairly well by the model (model: -21±17%, observation: -29±21%). The observational constraint on VOC emissions is found to be generally weak except for lower

33 latitudes. Results support an increase in surface ozone during the lockdown. In April, the

34 constrained model features a reasonable agreement with maximum daily 8 h average (MDA8)

35 ozone changes observed at the surface (r=0.43), specifically over central Europe where ozone

36 enhancements prevail (model: +3.73±3.94%, +1.79 ppbv, observation: +7.35±11.27%, +3.76

37 ppbv). The model suggests that physical processes (dry deposition, advection, and diffusion)

38 decrease MDA8 surface ozone in the same month on average by -4.83 ppbv, while ozone

39 production rates dampened by largely negative $J_{NO2}[NO_2]$-$k_{NO+O3}[NO][O_3]$ become less negative,

40 leading ozone to increase by +5.89 ppbv. Experiments involving fixed anthropogenic emissions

41 suggest that meteorology contributes to 42% enhancement in MDA8 surface ozone over the same

42 region with the remaining part (58%) coming from changes in anthropogenic emissions. Results

43 illustrate the capability of satellite data of major ozone precursors to help atmospheric models

44 capture ozone changes induced by abrupt emission anomalies.

45 **1. Introduction**

46   Continuous monitoring of air pollution by satellites can help our understanding of both

47 anthropogenic and biogenic variability and change caused by rapid economic recession

48 [Castellanos and Boersma, 2012] and regulations [Krotkov et al., 2016; Souri et al., 2020a]. Earth's

49 atmosphere has substantially become more polluted since the industrial era in comparison to its

50 original environmental condition [Li and Lin, 2015], thus any abrupt hiatus in anthropogenic (man-

51 made) emissions should result in an immediate impact on relatively short lifetime pollutants such

52 as nitrogen dioxide (NO_2), formaldehyde (HCHO), and tropospheric ozone (O_3). The beginning of

53 the global COVID-19 pandemic in early 2020 [Fauci et al., 2020] provided such an abrupt change

54 in human activities [Le Quéré et al., 2020]. A first step to fully understand how much of these

55 impacts are related to the pandemic lockdowns is to disentangle the physiochemical processes

56 determining their ambient concentrations. Unraveling those processes require precise, continuous

57 observations of physical and chemical states and emission rates, which are not routinely available

58 on global, continental and regional scales. Therefore, we resort to using a model realization

59 attempting to reproduce such an intricate system. Models without observational guidance are

60 incapable of numerically representing the real world [Lorenz, 1963], so our best option to improve

61 a model is to constrain some of its prognostic inputs using well-characterized observations.

62 Accordingly, the framework of this study is centered around inverse modeling and data

63 assimilation.

64   Significant attention has been given to documenting the lockdown-related changes in
65 atmospheric composition around the world using both in-situ and satellite observations [e.g.,
66 Sicard et al., 2020; Shi and Brasseur, 2020; Lee et al., 2020; Salma et al., 2020; Le Quéré et al.,
67 2020; He et al., 2020; Le et al., 2020; Miyazaki et al., 2020; Liu et al., 2020; Barré et al., 2020;
68 Goldberg et al., 2020; Ordóñez et al., 2020; Wyche et al., 2021; Bekbulat et al., 2020; Gaubert et
69 al., 2021; Sun et al., 2021]. The broad picture is consistent among these studies; the lockdown
70 drastically reduced the concentrations of NO_x, CO, and SO_2 and some types of particulate matter,
71 whereas the concentrations of several secondarily formed compounds such as ozone behaved in
72 non-linear ways due to emissions and/or meteorology.

73   The motivations of this study are to determine the capability of a regional model
74 constrained by satellite HCHO and NO_2 columns to capture near-surface pollution, and if local
75 ozone production rates are the driving factors for heightening ozone pollution during the 2020
76 lockdown. In other words, what physiochemical processes are associated with the elevated ozone?
77 How representative are satellite observations at capturing surface air quality through an inversion
78 context? Is meteorology the primary factor in shaping elevated ozone as suggested by Ordóñez et
79 al. [2020]?

80   To address these pivotal questions, it is desirable to constrain models using multi-species
81 observations because relationships between the atmospheric compounds such as HCHO and NO_2
82 are importantly intertwined [Marais et al., 2012; Valin et al., 2016; Wolfe et al., 2016; Souri et al.,
83 2020a,b]. Accordingly we build our inversion framework upon a non-linear joint analytical
84 inversion of NO_x and VOCs proposed in Souri et al. [2020a] using the TROPOspheric Monitoring
85 Instrument (TROPOMI) HCHO and NO_2 observations in Europe. Performing this type of
86 inversion not only enables us to precisely quantify the changes in emissions (along with its
87 uncertainty, as the inversion framework is analytical) but also paves the way for estimating the
88 resulting changes on different pathways of ozone.

89 **2. Measurements, Modeling, and Methods**
90   *2.1. Satellite Observations*
91   *2.1.1. TROPOMI NO_2*
92   We use daily offline S5P TROPOMI tropospheric NO_2 slant columns
93   [Copernicus Sentinel data processed by ESA and Koninklijk Nederlands
94   Meteorologisch Instituut (KNMI), 2019] derived from a two-step framework

involving DOAS spectral fitting in conjunction with a stratosphere/troposphere decoupler [Boersma et al., 2018]. The time periods of this study are March, April, and May 2020 and 2019. The data provide Jacobians of light intensity with respect to optical thickness (i.e., vertically-resolved scattering weights) which are dependent on scene surface reflectivity, the cloudiness of the assumed Lambertian clouds, and the sensor viewing geometry.

Aerosol effects on the scattering weights are not taken into consideration. Based on radiative transfer calculations and satellite-based aerosol products, Jung Y. et al [2019] and Cooper et al. [2019] observed small changes (<10%) in AMFs with and without considering the aerosol impacts in Europe in springtime. This tendency likely results from a low aerosol optical depth.

The 2019 TROPOMI observations used in this study have a spatial resolution of 7×3.5 km^2, whereas those in 2020 have a spatial resolution of 5.5×3.5 km^2. The NO$_2$ products for the study time period were produced by processor versions v01.02.02 (1 March 2019 – 20 March 2019) and v01.03.02 (20 March 2019 onward). The v01.03.02 processor includes an update to the FRESCO-S cloud algorithm and improvements to a quality flag variable. NO$_2$ validation from processors v01.02.02 and v01.03.02 shows similar biases and dispersion [Lambert et al., 2020], as do comparisons from before and after the pixel spatial resolution change [Verhoelst et al., 2021]. We extract good quality pixels based on the main quality flag (qa_flag) > 0.75, which removes retrievals flagged as bad and pixels over snow/ice or with cloud radiance fractions > 0.5, and resample them to our 15-km regional model (discussed later) using the bilinear interpolation. Since vertical column densities (VCDs) depend on assumed gas profile shape (i.e., they are quasi-observations), we recalculate those shape factors using profiles from our constrained chemical transport model. Shape factors are re-estimated by calculating the ratio of the vertical column of total air to the simulated vertical column of NO$_2$ multiplied by the mixing ratios of NO$_2$ profile from the regional model [Martin et al., 2002].

Satellite remote sensing observations are usually far more stable than they are accurate. This can make the data practical for measuring relative changes in

126   emissions, but may necessitate the use of a bias correction for absolute emissions

127   estimates. Moreover, the systematic and random errors associated with satellite

128   retrievals may differ markedly from location to location. It is therefore crucial to

129   thoroughly validate columns against independent observations. To this end, we

130   compile statistics reported in several validation studies focusing on the TROPOMI

131   tropospheric NO_2 product and summarize their findings in Table 1. The most

132   comprehensive global study to date is a comparison of TROPOMI tropospheric

133   NO_2 with that derived from 19 MAX-DOAS instruments [Verhoelst et al., 2021].

134   This study indicates there is a low bias in TROPOMI tropospheric NO_2 of -23 to -

135   37% relative to MAX-DOAS at clean to moderately polluted sites, and as large as

136   -51% at highly polluted sites. When considering all sites, the overall median bias

137   in this study was found to be -37%, with a dispersion of 3.5×10^{15} molec/cm^2

138   (defined as half of the 68% interpercentile). No obvious seasonal patterns were

139   found in the biases. These results are consistent with other validation studies which

140   have observed a low bias in TROPOMI tropospheric NO_2 [Chan et al., 2020; Griffin

141   et al., 2019; Judd et al., 2020]. A potential significant source of bias in polluted

142   regions is the relatively low spatial resolution (1×1°) TM5-MP prior profiles used

143   in the TROPOMI air mass factor calculation. Several validation studies have shown

144   the low bias in TROPOMI NO_2 can be reduced in polluted regions by 5-17%

145   through the use of higher spatial resolution model a priori profiles or other

146   improvements in the AMF calculation [Chan et al., 2020; Griffin et al., 2019; Judd

147   et al., 2020; Zhao et al., 2020].

148   Directly incorporating these numbers into an inversion model is

149   challenging, mainly because of spatiotemporal variability in the satellite errors.

150   Ideally, the relationship between errors and retrieval inputs (e.g., albedo, scene

151   radiance, profiles, etc.) would be used as an additional cost function in the

152   inversion, commonly known as variational bias correction [e.g., Auligné et al.,

153   2007]. In the absence of such relationships, we use the biases reported in the

154   validation studies.

155   In the case of NO_2, we uniformly scale up the satellite tropospheric columns

156   by 25%. This bias estimate is derived by first assuming a 37% low bias in the

157   columns over polluted regions as reported by Verhoelst et al. [2021]. In turn, this

158   low bias can be mitigated somewhat by the application of high spatial resolution

159   profiles in the air mass factor calculation, such as the ones used in this study. Table

160   1 summarizes the results from several TROPOMI validation studies at specific

161   locations that calculated NO_2 using model profiles with higher spatial resolution

162   than the operational TROPOMI ($1°×1°$) profiles (see Table 1 columns

163   "Modification" and "Modified Bias"). In these studies, modified columns show

164   increases ranging from 0 - 25%. Based on these results, we assume a low bias of

165   37% can be mitigated by ~12% through the use of high spatial resolution profiles,

166   for a resulting total low bias of 25%. This bias is likely not valid over pristine areas,

167   where validation studies show lower biases in TROPOMI NO_2 [Verhoelst et al.,

168   2021, Wang et al., 2020, Zhao et al., 2020]; nonetheless, we previously observed

169   in Souri et al. [2020a] that the low signal-to-noise ratios of those column amounts

170   resulted in small changes in the top-down emissions. We assume the errors of

171   observations originate from two main sources: i) the precision error provided with

172   the data ($e_{precision}$) and ii) a fixed error estimated from comparisons to in-situ

173   measurements (e_{const}). Mathematically, the final error is:

$$e_O^2 = e_{const}^2 + \frac{1}{n^2} \sum_{i=1}^{n} e_{precision,i}^2 \tag{1}$$

174   where n is the number of samples for a given grid and e_{const} equals to $1.1×10^{15}$

175   molec/cm^2 ($<6×10^{15}$ molec/cm^2) in clean regions and $3.5×10^{15}$ molec/cm^2

176   ($>=6×10^{15}$ molec/cm^2) in moderately to highly polluted regions. These regions are

177   defined based on the wide ranges reported in Verhoelst et al. [2021] ($3\text{-}14×10^{15}$

178   molec/cm^2 for moderately to highly polluted regions).

179   *2.1.2. MODIS AOD*

180   To improve the simulation of total aerosol mass, we use the collection 6

181   MODIS aerosol optical depth (AOD) from both Aqua (~ 13:30 LT) and Terra (~

182   10:30 LT) platforms over both land and ocean [Levy et al., 2013] (available at

183   https://ladsweb.modaps.eosdis.nasa.gov, access May 2020). We independently

184   validate all three major products, namely the deep blue, the dark target and a

185   combined dark blue products by comparing to AOD values measured by

AERONET over Europe at the same time period of this study. Only good and very good (qa>=2) pixels are selected for the comparison. The AERONET AOD data are computed based on the values at 500 nm and Angstrom Exponent in the 440-675 nm range. We collocate two datasets if they are within 10 km radius and less than 30 mins apart. The dark blue product results in the best agreement (r>0.87) with a high bias of <0.05 (Figure S3, and S4). This product is therefore chosen for the data assimilation. We remove the bias and assign the value of the covariance matrix of observations to the RMSE values obtained from the comparison.

2.2. Surface Measurements

UV photometry and chemiluminescence surface ozone and NO_2 measurements all over continental Europe are used to investigate possible changes in their concentrations induced by the lockdown (https://discomap.eea.europa.eu/map/fme/AirQualityExport.htm, access June 2020). The NO_2 chemiluminescence measurements are usually overestimated due to interferences from the NO_z family (PAN, organic nitrate, HNO_3, etc.). We assume that the interferences are not significantly different between the baseline and lockdown mainly due to relatively low photochemistry in early spring [Lamsal et al., 2008] compared to summertime. Additionally, the correction needs a careful evaluation of the model with regards to the NO_z family whose measurements are not available in this case study.

More than 6450 meteorological stations archived on NOAA's integrated surface database (https://www.ncei.noaa.gov/data/global-hourly/, access April 2020) are used to validate the performance of our weather model in terms of several prognostic inputs including ambient air temperature, air humidity, and U and V wind components.

2.3. WRF-CMAQ Modeling

The regional air quality simulations at 15×15 km^2 are carried out with the widely used CMAQ v5.2.1 (https://doi.org/10.5281/zenodo.1212601) in conjunction with WRF v3.9.1 [Skamarock et al. 2008] models. The models overlap and cover continental Europe and some portions of Africa and Middle East. The domain consists of 483 east-west, 383 north-south grids, and 37 unevenly spaced eta levels (Figure 1). The simulation time period is from March to May 2019 and 2020 (six months). Since IC/BC are taken from already spun-up National Centers for Environmental Prediction (NCEP) FNL (final) reanalysis and GEOS-Chem v12.9.3 (10.5281/zenodo.3974569) runs, we only spin up the models for the

month of February. The chemistry configuration of the CMAQ model mainly consists of CB05 with chlorine chemistry (gases) and AERO6 (aerosol). Hourly-basis biogenic emissions are processed by the offline standalone Model of Emissions of Gases and Aerosols from Nature (MEGAN) v2.1 model [Guenther et al., 2012] based on high-resolution plant functional maps made by Ke et al. [2012]. The biogenic emission factors are estimated based on the PFT-specific information provided in Guenther et al. [2012]. The biogenic VOCs include a wide range of compounds including isoprene, monoterpenes, aromatic VOCs, and methanol. Soil NO_x emissions are estimated by Yienger and Levy, [1999]. Lightning NO_x emissions are based on in-line calculations involving convective precipitation rates and cloud vertical distributions. Lightning NO_x emissions are not constrained in the model. Anthropogenic emissions are based on the Community Emissions Data System (CEDS) inventory in 2014 [Hoesly et al., 2018]. Diurnal scales are not considered for the anthropogenic emissions. We also output the CMAQ integrated process analysis quantifying the contribution of each process to the amount of compounds. The physical setting of WRF includes the Lin microphysics scheme [Lin et al., 1983], the Grell 3-D ensemble cumulus scheme [Grell and Dévényi, 2002], the RRTMG radiation scheme, ACM2 planetary boundary layer parametrization [Pleim, 2007], and Pleim-Xu land-surface scheme [Xiu and Pleim, 2001]. To minimize the deviation of the model from the reanalysis data, we turn on the grid nudging option with respect to wind, moisture, and temperature only outside of the PBL region. The inclusion of this option only outside of the PBL region is because we do not want the coarse reanalysis data wash out the relatively high-resolution dynamics. Moreover, leaf area index and the sea surface temperature are updated every 6 hours based on satellite measurements included in the reanalysis data. Extensive model evaluations based upon surface observations show a striking correspondence (Table S1, S2) which is indicative of reasonable energy budget and transport in our model.

2.4. Inverse Modeling and Data Assimilation

To adjust the bottom-up emission inventories, we follow a non-linear joint inversion method proposed in Souri et al. [2020a]. Briefly, a Gauss-Newton algorithm is utilized to incrementally solve the Bayes' quadratic function in analytical fashion. The posterior emissions are then derived by

$$\mathbf{x}_{i+1} = \mathbf{x}_a + \mathbf{G}[\mathbf{y} - F(\mathbf{x}_i) + K_i(\mathbf{x}_i - \mathbf{x}_a)] \tag{2}$$

where y is bias-corrected monthly-averaged TROPOMI NO_2 and HCHO observations (see S.A1), $\mathbf{x}_a$ (or $\mathbf{x}_0$) is the prior emissions, $\mathbf{x}_i$ is the posterior emission at the ith increment, F is the forward model (here WRF-CMAQ) to project the emissions onto columns space, $\mathbf{G}$ is the Kalman gain,

$$\mathbf{G} = \mathbf{S}_e \, K_i^T \left(K_i \mathbf{S}_e \, K_i^T + \mathbf{S}_o \right)^{-1} \tag{3}$$

and $K_i \, (= K(\mathbf{x}_i))$ is the Jacobian matrix calculated explicitly from the model using the finite difference method by perturbing separately NO_x and VOC emissions by 20%. The perturbations are applied for each iteration. The model outputs along with Jacobians and emissions are spatiotemporally co-registered with the observations. $\mathbf{S}_o$ and $\mathbf{S}_e$ are the error covariance matrices of the observations and emissions. Similar to Souri et al. [2020a], the prior errors in anthropogenic NO_x and VOCs emissions are set to 50% and 150%, respectively. In terms of the biogenic emissions, the errors are set to 200% for both NO_x and VOCs. The instrument covariance matrices are populated with squared-sum of the aforementioned errors based on the compilation of the validation studies and precision errors provided with the data (Eq.1). Both error matrices are assumed diagonal. The inversion window is monthly meaning we have three separate correction factors in months of March, April, and May. The covariance matrix of the a posteriori is calculated by:

$$\hat{\mathbf{S}}_e = (\mathbf{I} - \mathbf{G}\hat{K}) \mathbf{S}_e \tag{4}$$

where $\hat{K}$ is the Jacobian from the ith iteration. Here we iterate Eq.2 three times. The averaging kernels ($\mathbf{A}$) are given by:

$$\mathbf{A} = \mathbf{I} - \hat{\mathbf{S}}_e \mathbf{S}_e^{-1} \tag{5}$$

Not only does this method considers non-linear chemical feedback among NO_2-HCHO-NO_x-VOC by simultaneously incorporating the HCHO and NO_2 in the inversion framework, it also permits quantification of $\mathbf{A}$ that explicitly explains the amount of information obtained from the observation. Low $\mathbf{A}$ indicates low $\mathbf{G}$ making the a posteriori to be rather independent of the observational constraint.

An important caveat with this inversion system is that we do not take the model parameter error (such as errors in chemistry, cloud microphysics, and PBL) into account. To properly estimate the forward model parameter errors, one needs to calculate the

274   sensitivity matrix of the columns to the model parameters combined with the sensitivity

275   matrix of the columns to the emissions (K) [Rodgers, 2000]. The former calculation is

276   computationally expensive. Moreover, the spatiotemporal varying model parameter errors

277   may not be known in detail. The consequence of disregarding the model parameter errors

278   is an overconfidence in the top-down estimates (i.e., an overestimation of AKs).

279   We also correct total aerosol mass by daily assimilating the MODIS dark blue AOD

280   observations following the algorithm discussed in Jung et al. [2019]. Briefly, the

281   assimilation framework uses a modified optimal interpolation method adjusting uniformly

282   all relevant aerosol masses in a column as a function of a weighted-distance and appropriate

283   errors.

3. Results and Discussion

3.1. Variability of NO_2 columns seen by TROPOMI

286   We assess difference maps of NO_2 columns (and HCHO in S1) in 2020 with respect to

287 those in 2019 during the months of March, April and May. The difference maps along with the

288 absolute values of the tropospheric NO_2 columns are shown in Figure 2. Regardless of the year,

289 we observe a noticeable reduction in NO_2 as we approach warmer months which can be explained

290 by increases in OH concentrations (higher water vapor content, solar radiation, and O_3 levels),

291 faster vertical mixing due to larger sensible fluxes (more diluted columns for a given receptor due

292 having a greater chance of experiencing stronger winds in higher altitudes), and a reduction in

293 temperature-dependent light-duty diesel NO_x emissions [Grange et al., 2019]. This sequential

294 decline of NO_2 obscures the quantitative interpretation of the satellite observations in two ways:

295 first, as noted by Silvern et al. [2019], the free tropospheric background NO_2 levels, which are

296 highly uncertain, becomes comparable to those located at near-surface, and second, the relatively

297 lower signal-to-noise ratios reduce the amount of information that we can obtain for inverting NO_x

298 emissions (discussed later).

299   The anomaly map (2020 vs 2019) in March indicates pronounced decreases in tropospheric

300 NO_2 columns over several countries including France, Spain, Italy, and Germany (box A). In

301 contrast, we see increases in the magnitude of the NO_2 columns over some portions of the UK

302 excluding London (box B), northeastern Germany (box C), and Moscow, Russia (box D). A recent

303 study [Barré et al. 2020] observed roughly the same tendency which was attributable to

304 meteorological changes. While those changes are indeed an important piece of information, we

305 should recognize that the degree of the enforced restrictions varies temporally; moreover changes

306 in emission heavily rely on the dominant emission sector (e.g., mobile or industry). For instance,

307 according to TASS press [https://tass.com/society/1144123, accessed Sep 2020], Russian

308 governments did not take significant measures to control the virus before April 15, immediately

309 evident in the large NO_2 enhancement over Moscow in March (box D). During the next two months

310 (April and May), we observe a major turnaround over this city (box F and H). In May, the anomaly

311 of the tropospheric NO_2 suggests that the reduction in NO_x emissions abruptly experiences a hiatus

312 in central Europe (box G). However it is crucial to note that these maps are based upon sporadic

313 clear-sky pixels that might obscure the full portrayal of emissions changes happening throughout

314 the period (discussed later).

315   ***3.2. Top-Down estimates of NO_x emissions***

316   Following the inversion and the data assimilation frameworks, we adjust the total amounts

317 of VOC, NO_x emissions, and aerosols mass using TROPOMI HCHO, NO_2 and MODIS AOD

318 observations. We focus on the topic of gas phase chemistry (i.e., ozone and its precursors) implying

319 that the aerosol data assimilation is carried out to partially remove errors associated with radiation

320 [e.g., Jung et al., 2019] or heterogenous chemistry [Jacob, 2000]; therefore, the aspect of aerosol

321 changes induced by the lockdown will be examined in a separate study. Furthermore, we observe

322 a relatively weak observational constraint from TROPOMI HCHO on VOC emissions, especially

323 in higher latitudes; accordingly, the relevant discussion on this subject is presented in S2.

324   The spatial distributions of magnitude of the top-down NO_x and their corresponding

325 changes and averaging kernels are shown in Figure 3. Moreover, the monthly values of the a

326 posteriori and the a priori are shown in Figure S5 and S6. It is worth emphasizing that we use

327 identical prior values in terms of anthropogenic emissions in both years.

328   According to Figure 3, large averaging kernels associated with NO_x emissions are confined

329 in high-emitting regions suggesting that the most valid estimates can be found in areas undergoing

330 strong TROPOMI NO_2 signals. We observe an improvement in the statistics associated with

331 simulated surface NO_2 using the posterior emissions compared to the surface measurements in

332 many places around Europe with an exception to northeastern Germany where TROPOMI NO_2

333 observations deviates the model from the measurements (Figs S9-S12; Tables S3, S4). The large

334 underestimation of the model in terms of surface NO_2 concentrations is most likely due to the

335 underestimation of the CEDS inventory [e.g., Figure 12 in Sun et al., 2021]. However, it is worth

336 noting that the disagreements between the model and the surface measurements do not solely
337 reflect the uncertainty in the emissions. A major complication arises from the fact that the point
338 measurements represent concentrations locally, whereas the model grids (15×15 km^2) are (at best)
339 the average of infinitesimal points integrated over the grid space. Essentially, no one should expect
340 that these quantities will completely line up, unless one transforms the point measurements to the
341 grids (i.e., rasterization) by carefully modeling the spatial auto-correlation (or semivariograms) of
342 the point data [Souri et al., 2021]. Additionally, there is uncertainty about the chemical mechanism
343 utilized in the model. In particular, Souri et al. [2017] observed a large overestimation ($\sim$ factor 4)
344 of daily-averaged total nitrate ($HNO_3 + NO_3^-$) in the CB05/AERO6 mechanism despite moderately
345 reasonable nitrate (NO_3^-) simulations. This was attributed to a large overestimation of N_2O_5
346 hydrolysis rate [Bertram and Thornton, 2009] which is the primary loss pathway of NO_x in low
347 photochemically active regions [Shah et al., 2020]. The interferences from the NO_z family on the
348 surface measurements might be still present in springtime in midlatitudes ($\sim$10-30%) [Lamsal et
349 al., 2008]. Last but not the least, the PBL parameterization controlling the level of vertical mixing
350 rates has errors primarily due to soil moisture not being observationally constrained in the model
351 [Huang et al., 2021].

352 The discrepancies between the simulated tropospheric NO_2 columns versus TROPOMI are
353 mitigated by the inversion (Figure S13 and S14). Immediately apparent in Figure 3 is a strong
354 correlation between anomaly maps of TROPOMI tropospheric NO_2 (Figure 2) and those of top-
355 down emissions. We observe reductions in NO_x emissions in March (14-31%) in several major
356 cities including Paris, London, Madrid, and Milan; the reductions further expand to Rome,
357 Brussels, Frankfurt, Warsaw, Kyiv, Moscow, and Belgrade with higher magnitudes (34-51%) in
358 April. In general, the level of NO_x reduction is somewhat higher in April relative to months of
359 March and May possibly due to temporal variabilities associated with the restrictions; for example,
360 UK and Poland governments enforced the restrictions starting in the last week of March to the
361 middle of April (see Figure S1 in Okruszek et al. [2020]; https://www.bbc.com/news/uk-
362 51981653, accessed in March 2020). The decreased anthropogenic NO_x emissions in the strait of
363 Gibraltar and Alboran Sea reveal reportedly reduced ship activities [United Nations Conference
364 on Trade and Development Report, Accessed Dec 2020]. The numbers in May indicate that several
365 countries in central and eastern Europe (shown in box G in Figure 2) likely eased coronavirus

366   lockdown restrictions, a picture that has yet to be verified by surface measurements (discussed

367   later).

3.3. Disparities in near-surface concentrations suggested by the constrained model versus

        those by in-situ measurements

3.3.1. NO$_2$

371   It is necessary to examine whether the constrained model can precisely represent the

372   changes observed by surface measurements. Several factors can complicate this analysis: i) having

373   overconfidence in the constrained model where the satellite observations used were uncertain; this

374   problem can be addressed by considering grid cells whose averaging kernels are above a threshold

375   (here 0.5), ii) not accounting for spatial representativity function when it comes to directly

376   comparing two datasets at different scales (i.e., point measurements vs the model grids); a

377   statistical construction of the spatial representivity function [Janic et al., 2016; Souri et al., 2021]

378   requires a dense observational network so that we can build a semivariogram; instead, we only

379   consider model grid cells having more than two stations; those observations then are then averaged,

380   iii) interferences of the NO$_z$ family on NO$_2$ chemiluminescence measurements [Dickerson et al.,

381   2019] which can be partly discounted when calculating differences, iv) model uncertainties,

382   especially with respect to turbulent and convective fluxes that are heavily determined by

383   representing local heterogeneity of forces and non-hydrostatic dynamics [Emanuel, 1994], all of

384   which are challenging to fully resolve in a 15-km resolution.

385   With these caveats in mind, we plot the daily-averaged changes of surface NO$_2$

386   concentrations in 2020 relative to 2019 derived by the model and the European air quality network

387   for the months of March, April, and May (Figure 4). Large gaps in Figure 4 are caused by

388   considering grid cells with averaging kernels>0.5 and number of samples>2. The constrained

389   model correlates reasonably well with the changes observed by the surface measurements in April,

390   but it fails to fully reflect those in March and May. The surface measurements in March reinforce

391   increases (or negligible changes) in NO$_2$ in northeastern Germany and UK, although the

392   magnitudes are not as large as those suggested by the model (and TROPOMI NO$_2$ columns). A

393   number of factors can contribute to these large discrepancies: i) the surface measurements were

394   present throughout the month of March, whereas TROPOMI data were frequently absent due to

395   cloudiness resulting in some degree of temporal representativity issues; ii) the statistics used for

396   the TROPOMI bias-correction may not always hold true, since each individual pixel can deviate

397   from the norm of the reported biases; iii) the shape of NO_2 profiles simulated by the WRF-CMAQ

398   can sometimes be uncertain due to errors in the PBL parameterization or the difficulties with

399   resolving the non-hydrostatic components (where vertical motions are comparable to horizontal

400   ones) [e.g., Pouyaei et al., 2021]; this complication can result in unrealistic changes in the columns.

401   The constrained model tends to consistently underrepresent the decline in NO_2 in March (model:

402   -11±21%, observation: -19±16%), April (model: -21±17%, observation: -29±21%), and May

403   (model: -12±18%, observation: -25±20%). The frequency of TROPOMI data heavily impacted by

404   cloudiness is an important factor effectively leading to the underrepresentation of the model in a

405   course of a month. Figure 5 depicts the average number of days that TROPOMI was able to sample

406   on in both years (individual years are shown in Figure S18 and S19). There is a strong degree of

407   correlation between the frequency of the data and the discrepancy between the model versus the

408   surface observations. This is especially the case for May when we see too few days to be able to

409   realistically reproduce NO_2 changes.

410   Given the reasonable performance of our model at reproducing the changes observed over

411   the surface in April, a result of abundant samples from TROPOMI, we only focus on this month

412   for the subsequent analysis.

413   ***3.3.2. Ozone***

414   Figure 6 depicts the changes in maximum daily 8 h average (MDA8) surface ozone

415   concentrations suggested by the measurements and the constrained model in April 2020 with

416   respect to 2019. Immediately obvious from the observations is the elevated surface ozone

417   concentrations up to 32% in places where NO_x emissions drastically decreased such as Germany,

418   Italy, France, UK, Switzerland, and Belgium (shown as box L). This tendency potentially driven

419   by ozone chemistry [Sicard et al., 2020a; Shi and Brasseur, 2020; Grange et al. 2020; Salma et al.,

420   2020; Lee et al., 2020] and/or meteorology [Lee et al., 2020; Wyche et al., 2021; Ordóñez et al.,

421   2020] has drawn much attention. The challenge is to set up a model that is the characteristic of

422   such a complex tendency [e.g., Parrish et al., 2014]. Encouragingly, our constrained model does

423   have skill in describing the ozone enhancements over the whole domain (r=0.43). In the proximity

424   of central Europe (shown as box L), the enhanced MDA8 ozone concentration observed by the

425   observations is 7.35±11.27% (+3.76 ppbv) which is nearly a factor of two larger than that of the

426   model (3.73±3.94%, +1.79 ppbv).

427   We plot the simulated MDA8 surface ozone concentrations in April 2020 (lockdown),

428   April 2019 (baseline), and their differences in Figure 7. Surface ozone concentrations show a

429   strong latitudinal gradient with lower values in higher latitudes, underscoring the importance role

430   of solar radiation in the formation of ozone. Meanwhile, the Mediterranean basin is prone to

431   elevated concentrations of ozone resulting from different factors including calm weather, the

432   transport from neighboring countries, atmospheric recirculation in coastal environments, and local

433   emissions [Lelieveld et al., 2002]. While we observe a strong variability in the difference map,

434   signaling various sources and sinks (discussed later), three distinctive features in 2020 in

435   comparison to 2019 are evident: i) higher concentrations over the central Europe (up to 5 ppbv),

436   ii) lower concentrations in eastern Europe (-2.67±1.65 ppbv) due to the 2019 biomass burning

437   activities (see S1 and S2) and larger snow cover fraction accelerating photolysis [e.g.,

438   Rappenglück et al., 2014], and iii) lower values in the Iberian Peninsula (-0.51±1.41 ppbv)

439   [Ordóñez et al., 2020].

440   While the remaining model uncertainty could be either improved or characterized by

441   including more observations (if available), reconfiguring the physiochemical mechanisms used,

442   and constraining chemical boundary conditions, it is imperative to gauge the contribution of each

443   process (i.e., transport, chemistry, etc.) in forming ozone changes. Here we mainly make use of

444   the CMAQ process analysis. A direct use of the process analysis output (in unit of ppbv hr^{-1}) can

445   be confusing as both physiochemical processes and underlying concentrations are inextricably

446   linked together. To be able to isolate each process (in unit of hr^{-1}), we normalize the outputs by

447   ozone concentrations. We average each process at the same hours used in calculating MDA8.

448   Figure 8 shows the major model processes, namely horizontal transport (horizontal advection plus

449   diffusion), vertical transport (vertical advection plus diffusion), dry deposition, and chemistry in

450   2020, 2019, and their differences. Positive (negative) values indicate a source (sink) for ozone.

451   Regarding the horizontal transport, the values mostly follow the transport pattern and are

452   dependent on whether the advected air mass is more or less polluted. The vertical transport

453   correlates with the PBLH which is an indicator of the atmospheric stability and turbulence,

454   although we should not rule out the impact of the subgrid convective transport that can occur

455   sporadically. Low PBLHs are usually associated with more stable (or sometimes capping

456   inversion) and weaker vertical mixing [e.g., Nevius and Evans, 2018]. Vertical transport which is

457   majorly dictated by the vertical diffusion is by far the most influential factor in the magnitude of

458 ozone [e.g., Cuchiara et al., 2014]. In contrast to NO_2 and HCHO, a stronger vertical diffusion

459 increases surface ozone due to positive gradients of ozone with respect to altitude. However, the

460 aerodynamic resistance controlling dry deposition velocity [Seinfield and Pandis, 2006] is also a

461 function of turbulent transport. For example, during daytime, intensified turbulence exposes more

462 pollution to surface deposition. It is because of this reason that we see the dry deposition process

463 largely counteracting vertical transport. This will leave the chemistry process the major driver of

464 the ozone changes.

465   We separately sum the quantities of the physical processes and PO_3 contributing to MDA8

466 surface ozone changes binned to box L. The physical processes lead to -4.83 ppbv changes in the

467 MDA8 ozone mainly due to a relatively larger dry deposition in 2020, whereas $P(O_3)$ contributes

468 to +5.89 ppbv. The net effect is +1.06 ppbv which is slightly smaller than the simulated changes

469 in MDA8 ozone in this region (+1.79 ppbv). This apparent discrepancy is caused by the differences

470 in boundary and initial conditions which are not quantifiable by the process analysis and would

471 require additional sensitivity test. Nonetheless, we believe these numbers should provide

472 convincing evidence on the fact that chemistry has promoted the enhancements of surface ozone

473 during the lockdown.

474   Chemistry is also a function of meteorology, specifically solar radiation and temperature.

475 A typical scenario to isolate emissions from meteorology is by running the model with fixed

476 anthropogenic emissions (and boundary conditions) and subtracting the outputs from the variable

477 emission output. Figure 9 shows the contribution of anthropogenic emissions (VOCs and NO_x) to

478 the changes seen over the surface. The anthropogenic emissions make up roughly 58% of the

479 changes. The map is strongly in line with the changes in NO_x emissions constrained by TROPOMI.

480 The impact of meteorology plus biogenic changes (the former is dominant) highly correlates with

481 anomalies in both surface air temperature and photolysis rates dictated by synoptic conditions

482 (Figure S17). We observe negligible ozone changes due to emissions over Iberian Peninsula

483 reinforcing the significance of the meteorological impacts [Ordóñez et al., 2020].

484   **3.4. Ozone chemistry**

485   Figure 10 shows the numerically-solved ozone production rates (PO_3) simulated by the

486 constrained model during the MDA8 hours period. We observe positive PO_3 in less polluted areas

487 and eastern Europe where biomass burning activities occurred in 2019 (see S1 and S2), while

488 negative PO_3 in major cities. Negative values in PO_3 are indicative of either loss in O_3 or O_3-NO-

489   NO_2 partitioning. The difference in PO_3 between the two years suggests that the ozone

490   enhancement in box L is caused by a reduction in negative PO_3 in 2020 over major cities compared

491   to 2019. To examine which pathways are contributing to this pattern, we attempt to analytically

492   reproduce the numerically-solved PO_3 (Figure 10) through two different equations: the first

493   equation widely applied in photochemically active environments follows [Kleinman et al., 2002]:

$$P(O_3) = k_{HO_2+NO}[HO_2][NO] + \sum k_{RO_{2i}+NO}[RO_{2i}][NO]$$
$$- k_{OH+NO_2+M}[OH][NO_2][M] - k_{HO_2+O_3}[HO_2][O_3]$$
$$- k_{OH+O_3}[OH][O_3] - k_{O(^1D)+H_2O}[O(^1D)][H_2O] - L(O_3$$
$$+ VOCs) \tag{6}$$

494   This equation yields negative values only if the O_3 loss pathways including NO_2+OH, HO_x+O_3 ,

495   O^1D+H_2O and O_3+VOCs dominate over the first two terms. The second equation which is

496   independent of RO_2 and HO_2 concentrations [Thornton et al., 2002], is:

$$P(O_3) = jNO_2[NO_2] - k_{NO+O_3}[O_3][NO] \tag{7}$$

497   In summer, this equation tends to be positive during early afternoon, almost zero during afternoon

498   (steady-state), and negative in early morning (or night) in which the second term (O_3 titration) is

499   leading. Any abrupt changes in NO_x and VOC, and photolysis can directly affect Eq.7 moving PO_3

500   out of the diel steady-state. The assumption of the steady-state (PO_3 from Eq.7 equals to zero) is

501   also not valid if an air parcel is in the vicinity of high-emitting NO_x sources [Thornton et al., 2002].

502   Figure 11 displays the reactions rates of each individual component involved in Eq.6

503   averaged during the MDA8 hours. HO_2+NO is the dominant chemical source of ozone correlating

504   well with the changes in NO_x and prevailing chemical conditions regimes (NO_x-sensitive vs VOC-

505   sensitive). Souri et al. [2020a] found the reaction of RO_2+NO to be primarily dependent on VOCs.

506   Likewise, we observe a strong degree of correlation between the anomaly of RO_2+NO and that of

507   VOCs (Figure S1 and S2). Figure 11 indicates that the chemical pathways of ozone loss are rather

508   constant between the two years; therefore the largely negative PO_3 over urban areas shown

509   previously in Figure 10 is not reproducible using this equation. Figure 12 shows the reactions rates

510   of $J_{NO2}[NO_2]$, $k_{NO+O3}[NO][O_3]$, and the difference during the MDA8 hours. The difference maps

511   replicate the largely negative PO_3 over cities suggesting that we are not in the diel steady-state,

512   and O_3 titration is prevailing due to relatively low photochemistry in the springtime. Table 2 lists

513   the averaged reactions rates involved in Eq.6 and 7 along with the numerically-solved PO_3 shown

514 in Figure 10 over box L. These numbers suggest that the major chemical pathways of enhanced

515 ozone are through $J_{NO2}[NO_2]$ and $k_{NO+O3}[NO][O_3]$, implying that O_3-NO-NO_2 partitioning is more

516 consequential than other chemical pathways. This analysis strongly coincides with Lee et al.

517 [2020] and Wyche et al. [2021] who observed roughly constant O_3+NO_2 concentrations over the

518 UK before and during the lockdown 2020.

519 **4. Summary**

520 The slowdown in human activities due to the COVID-19 pandemic had a large impact on

521 air pollution over Europe [Barré et al. 2020; Siccard et al., 2020; Sun et al., 2021]. Satellite

522 monitoring systems with large spatial coverage help shed light on the spatial and temporal extent

523 of those impacts. The relationships between satellite-derived columns and near-surface emissions

524 have proven difficult to fully establish without using realistic models, capable of providing insights

525 on the convoluted processes involving chemistry, dynamics, transport, and photochemistry and

526 therefore help with deciphering what anomaly maps of satellite concentrations are suggesting [e.g.,

527 Goldberg et al., 2020]. To address these challenges, we jointly constrained NO_x and VOC

528 emissions using TROPOMI HCHO and NO_2 columns following a non-linear Gauss Newton

529 method developed in Souri et al. [2020a], in addition to assimilating MODIS AOD observations

530 based on Jung et al. [2019]. The constrained emissions also permitted investigating the

531 simultaneous effects of physiochemical processes contributing to ozone formation, illuminating

532 the complexities associated with non-linear chemistry.

533 Several implications of the derived emissions for the months of March, April, and May

534 2020 (lockdown) relative to those in 2019 (baseline) were investigated. First, as previously

535 reported [Sicard et al., 2020; Barré et al. 2020], we observed a significant reduction in NO_x in

536 March (14-31%) in several major polluted regions including Paris, London, Madrid, and Milan.

537 The reductions were further seen in other cities such as Rome, Brussels, Frankfurt, Warsaw,

538 Belgrade, Kyiv, and Moscow (34-51%) in April. Second, NO_x emissions decreased drastically in

539 April rather than March in UK, Moscow, and Poland due to the timeline of restrictions. Third, the

540 changes in NO_x suggested by TROPOMI NO_2 and the constrained model over northeastern

541 Germany in March and Central/Eastern Europe in May were unrealistic, possibly due to

542 observations or the model issues. Fourth, we observed a weak observational constraint on VOC

543 emissions from TROPOMI HCHO except for lower latitudes whose values were dictated by air

544 temperature.

545   The constrained model calculations gave good representations of near-surface NO_2
546   changes in April (model: -21±17%, observation: -29±21%) in places where the top-down estimates
547   are strongly constrained by TROPOMI (averaging kernels > 0.5), but inferior representations in
548   other months, especially in May (model: -12±18%, observation: -25±20%). This tendency mainly
549   arose from TROPOMI observation frequencies; too few days (10-26% out of a month) in May due
550   to cloudiness precluded the determination of realistic NO_x emission changes.

551   We observed surface MDA8 ozone increase from both model and measurements in April
552   2020 with respect to the baseline. Comparisons of calculation by the constrained model in terms
553   of MDA8 surface ozone found a reasonable agreement with observations in the proximity of
554   central Europe in April (model: +3.73±3.94%, +1.79 ppbv, observation: +7.35±11.27%, +3.76
555   ppbv). These comparisons indicate that the performance of the constrained model to reproduce the
556   ozone enhancement feature is promising, suggesting fruitful information in TROPOMI, although
557   reasons behind the underestimation of the enhancement remained unexplained. It was clear that
558   the dominantly negative ozone production rates dictated by O_3-NO-NO_2 partitioning ($J_{NO2}[NO_2]$-
559    $k_{NO+O3}[NO][O_3]$) became less negative primarily due to the reduced NO_x emissions in urban areas
560   where O_3 titration occurred. This tendency was in agreement with studies of Lee et al. [2020] and
561   Wyche et al. [2021]. We found negligible differences in ozone production from $[HO_2+RO_2][NO]$
562   and ozone loss from O^1D+H_2O and O_3+HO_x between the two years suggesting photochemistry
563   was rather low in the springtime over Europe.

564   We further quantified the contributions of physical processes (transport, diffusion and dry
565   deposition) and chemistry to the formation/loss of ozone using the integrated process rates. The
566   physical processes decreased MDA8 ozone by -4.83 ppbv resulting from relatively larger dry
567   deposition in 2020, whereas chemistry (ozone production) augmented ozone levels by +5.89 ppbv,
568   indicating that rising ozone was primarily impacted by changes in chemistry. Enhanced air
569   temperature and photolysis in 2020, both of which were well captured in our model, also affected
570   chemistry. Experiments with fixed anthropogenic emissions underwent significant enhancement
571   in surface MDA8 ozone over central Europe, but those only contribute to 42% of the total
572   enhancement indicating that anthropogenic emissions were the major factor.

573   The results shown here reveal previously unquantified characteristics of ozone and its
574   precursors emission changes during the lockdown 2020 in Europe. We have been able to measure
575   the amount of changes along with the level of confidence in NO_x (and partly VOC emissions)

576 using a state-of-the-art inversion technique by leveraging satellite observations, which in turn,
577 allowed us to unravel the physiochemical processes contributing to increased ozone in Europe.
578 Unless a comprehensive air quality campaign targeting COVID-19 related lockdown is available,
579 we recommend that the impact of lockdown on air pollution should be examined through the lens
580 of well-established models constrained by publicly available data, especially those from space in
581 less cloudy environments.

Author contributions

583 AHS designed the research, analyzed the data, conducted the inverse modeling and atmospheric
584 modeling (for CMAQ, GEOS-Chem, WRF, and MEGAN), made all figures, and wrote the paper.
585 JB validated WRF-CMAQ model and reformatted the surface observation files. CRN and GGA
586 did literature review regarding the TROPOMI validation. YJ validated MODIS AOD. DW helped
587 with implementing the AOD assimilation framework. KC, JM, and XL guided the discussion. All
588 authors contributed to discussion and edited the paper.

Data availability

590 The atmospheric inversion data are publicly available from Souri et al. [2021]. The model outputs
591 are available upon the request from ahsouri@cfa.harvard.edu. The links on where to download
592 surface and satellite observations that are used in this study are already provided in the text.

Acknowledgments

594 Amir H. Souri acknowledges supports from the Smithsonian Astrophysical Observatory (SAO)
595 Scholarly Award (40488100AA50203), MethaneSAT LLC, and Environmental Defense Fund. J.
596 Bak acknowledges Basic Science Research Program through the National Research Foundation of
597 Korea (NRF) funded by the Ministry of Education (2020R1A6A1A03044834). Both calculations
598 and simulations are done on the Smithsonian Institution High-Performance Cluster (SI/HPC)
599 (https://doi.org/10.25572/SIHPC). The views expressed in this manuscript are those of the authors
600 alone and do not necessarily reflect the views and policies of the U.S. Environmental Protection
601 Agency. EPA does not endorse any products or commercial services mentioned in this publication.

602

603

References

Auligné, T., McNally, A. P., and Dee, D. P.: Adaptive bias correction for satellite data in a
 numerical weather prediction system, Quarterly Journal of the Royal Meteorological
 Society, 133, 631–642, https://doi.org/10.1002/qj.56, 2007.

Barré, J., Petetin, H., Colette, A., Guevara, M., Peuch, V.-H., Rouil, L., Engelen, R., Inness, A.,
 Flemming, J., Pérez García-Pando, C., Bowdalo, D., Meleux, F., Geels, C., Christensen,
 J. H., Gauss, M., Benedictow, A., Tsyro, S., Friese, E., Struzewska, J., Kaminski, J. W.,
 Douros, J., Timmermans, R., Robertson, L., Adani, M., Jorba, O., Joly, M., and
 Kouznetsov, R.: Estimating lockdown-induced European NO2 changes using satellite and
 surface observations and air quality models, Atmospheric Chemistry and Physics, 21,
 7373–7394, https://doi.org/10.5194/acp-21-7373-2021, 2021.

Baudic, A., Gros, V., Sauvage, S., Locoge, N., Sanchez, O., Sarda-Estève, R., Kalogridis, C.,
 Petit, J.-E., Bonnaire, N., Baisnée, D., Favez, O., Albinet, A., Sciare, J. and Bonsang, B.:
 Seasonal variability and source apportionment of volatile organic compounds (VOCs) in
 the Paris megacity (France), Atmospheric Chemistry and Physics, 16(18), 11961–11989,
 https://doi.org/10.5194/acp-16-11961-2016, 2016.

Bekbulat, B., Apte, J. S., Millet, D. B., Robinson, A. L., Wells, K. C., Presto, A. A., and
 Marshall, J. D.: Changes in criteria air pollution levels in the US before, during, and after
 Covid-19 stay-at-home orders: Evidence from regulatory monitors, Science of The Total
 Environment, 769, 144693, https://doi.org/10.1016/j.scitotenv.2020.144693, 2021.

Bertram, T. H. and Thornton, J. A.: Toward a general parameterization of N2O5 reactivity on
 aqueous particles: the competing effects of particle liquid water, nitrate and chloride, 9,
 8351–8363, https://doi.org/10.5194/acp-9-8351-2009, 2009.

Boersma, K. F., Eskes, H. J., Richter, A., De Smedt, I., Lorente, A., Beirle, S., van Geffen, J. H.
 G. M., Zara, M., Peters, E., Van Roozendael, M., Wagner, T., Maasakkers, J. D., van der
 A, R. J., Nightingale, J., De Rudder, A., Irie, H., Pinardi, G., Lambert, J.-C. and
 Compernolle, S. C.: Improving algorithms and uncertainty estimates for satellite NO2
 retrievals: results from the quality assurance for the essential climate variables
 (QA4ECV) project, Atmospheric Measurement Techniques, 11(12), 6651–6678,
 https://doi.org/10.5194/amt-11-6651-2018, 2018.

Castellanos, P. and Boersma, K. F.: Reductions in nitrogen oxides over Europe driven by
 environmental policy and economic recession, Scientific Reports, 2(1), 265,
 https://doi.org/10.1038/srep00265, 2012.

Chan, K. L., Wiegner, M., van Geffen, J., De Smedt, I., Alberti, C., Cheng, Z., Ye, S. and Wenig,
 M.: MAX-DOAS measurements of tropospheric NO2 and HCHO in Munich and the
 comparison to OMI and TROPOMI satellite observations, Atmospheric Measurement
 Techniques, 13(8), 4499–4520, https://doi.org/10.5194/amt-13-4499-2020, 2020.

Cooper, M. J., Martin, R. V., Hammer, M. S., and McLinden, C. A.: An Observation-Based
 Correction for Aerosol Effects on Nitrogen Dioxide Column Retrievals Using the
 Absorbing Aerosol Index, 46, 8442–8452, https://doi.org/10.1029/2019GL083673, 2019.

Copernicus Sentinel data processed by ESA, Koninklijk Nederlands Meteorologisch Instituut
 (KNMI) (2019), Sentinel-5P TROPOMI Tropospheric NO2 1-Orbit L2 5.5km x 3.5km,
 Greenbelt, MD, USA, Goddard Earth Sciences Data and Information Services Center
 (GES DISC), Accessed: [Data Access Date], https://doi.org/10.5270/S5P-s4ljg54

Cuchiara, G. C., Li, X., Carvalho, J. and Rappenglück, B.: Intercomparison of planetary
    boundary layer parameterization and its impacts on surface ozone concentration in the
    WRF/Chem model for a case study in Houston/Texas, Atmospheric Environment, 96,
    175–185, https://doi.org/10.1016/j.atmosenv.2014.07.013, 2014.

Dickerson, R. R., Anderson, D. C. and Ren, X.: On the use of data from commercial NOx
    analyzers for air pollution studies, Atmospheric Environment, 214, 116873,
    https://doi.org/10.1016/j.atmosenv.2019.116873, 2019.

Emanuel, K. A.: Atmospheric Convection, 1st edition., Oxford University Press, New York.,
    1994.

Fauci, A. S., Lane, H. C. and Redfield, R. R.: Covid-19 — Navigating the Uncharted, New
    England Journal of Medicine, 382(13), 1268–1269,
    https://doi.org/10.1056/NEJMe2002387, 2020.

Gaubert, B., Bouarar, I., Doumbia, T., Liu, Y., Stavrakou, T., Deroubaix, A., Darras, S.,
    Elguindi, N., Granier, C., Lacey, F., Müller, J.-F., Shi, X., Tilmes, S., Wang, T., and
    Brasseur, G. P.: Global Changes in Secondary Atmospheric Pollutants During the 2020
    COVID-19 Pandemic, 126, e2020JD034213, https://doi.org/10.1029/2020JD034213,
    2021.

Goldberg, D. L., Anenberg, S. C., Griffin, D., McLinden, C. A., Lu, Z. and Streets, D. G.:
    Disentangling the Impact of the COVID-19 Lockdowns on Urban NO2 From Natural
    Variability, Geophysical Research Letters, 47(17), e2020GL089269,
    https://doi.org/10.1029/2020GL089269, 2020.

Grange, S. K., Farren, N. J., Vaughan, A. R., Rose, R. A. and Carslaw, D. C.: Strong
    Temperature Dependence for Light-Duty Diesel Vehicle NOx Emissions, Environ. Sci.
    Technol., 53(11), 6587–6596, https://doi.org/10.1021/acs.est.9b01024, 2019.

Grell, G. A. and Dévényi, D.: A generalized approach to parameterizing convection combining
    ensemble and data assimilation techniques, Geophysical Research Letters, 29(14), 38-1-
    38–4, https://doi.org/10.1029/2002GL015311, 2002.

Griffin, D., Zhao, X., McLinden, C. A., Boersma, F., Bourassa, A., Dammers, E., Degenstein,
    D., Eskes, H., Fehr, L., Fioletov, V., Hayden, K., Kharol, S. K., Li, S.-M., Makar, P.,
    Martin, R. V., Mihele, C., Mittermeier, R. L., Krotkov, N., Sneep, M., Lamsal, L. N.,
    Linden, M. ter, Geffen, J. van, Veefkind, P. and Wolde, M.: High-Resolution Mapping of
    Nitrogen Dioxide With TROPOMI: First Results and Validation Over the Canadian Oil
    Sands, Geophysical Research Letters, 46(2), 1049–1060,
    https://doi.org/10.1029/2018GL081095, 2019.

Guenther, A. B., Jiang, X., Heald, C. L., Sakulyanontvittaya, T., Duhl, T., Emmons, L. K. and
    Wang, X.: The Model of Emissions of Gases and Aerosols from Nature version 2.1
    (MEGAN2.1): an extended and updated framework for modeling biogenic emissions,
    Geoscientific Model Development, 5(6), 1471–1492, https://doi.org/10.5194/gmd-5-
    1471-2012, 2012.

He, G., Pan, Y. and Tanaka, T.: The short-term impacts of COVID-19 lockdown on urban air
    pollution in China, Nature Sustainability, 3(12), 1005–1011,
    https://doi.org/10.1038/s41893-020-0581-y, 2020.

Hoesly, R. M., Smith, S. J., Feng, L., Klimont, Z., Janssens-Maenhout, G., Pitkanen, T., Seibert,
    J. J., Vu, L., Andres, R. J., Bolt, R. M., Bond, T. C., Dawidowski, L., Kholod, N.,
    Kurokawa, J., Li, M., Liu, L., Lu, Z., Moura, M. C. P., O'Rourke, P. R. and Zhang, Q.:
    Historical (1750–2014) anthropogenic emissions of reactive gases and aerosols from the

Community Emissions Data System (CEDS), Geoscientific Model Development, 11(1), 369–408, https://doi.org/10.5194/gmd-11-369-2018, 2018.

Huang, M., Crawford, J. H., DiGangi, J. P., Carmichael, G. R., Bowman, K. W., Kumar, S. V., and Zhan, X.: Satellite soil moisture data assimilation impacts on modeling weather variables and ozone in the southeastern US – Part 1: An overview, 21, 11013–11040, https://doi.org/10.5194/acp-21-11013-2021, 2021.

Jacob, D. J.: Heterogeneous chemistry and tropospheric ozone, Atmospheric Environment, 34(12), 2131–2159, https://doi.org/10.1016/S1352-2310(99)00462-8, 2000.

Jacobson, M. Z.: Fundamentals of Atmospheric Modeling, 2nd ed., Cambridge University Press, Cambridge., 2005.

Janjić, T., Bormann, N., Bocquet, M., Carton, J. A., Cohn, S. E., Dance, S. L., Losa, S. N., Nichols, N. K., Potthast, R., Waller, J. A. and Weston, P.: On the representation error in data assimilation, Quarterly Journal of the Royal Meteorological Society, 144(713), 1257–1278, https://doi.org/10.1002/qj.3130, 2018.

Judd, L. M., Al-Saadi, J. A., Szykman, J. J., Valin, L. C., Janz, S. J., Kowalewski, M. G., Eskes, H. J., Veefkind, J. P., Cede, A., Mueller, M., Gebetsberger, M., Swap, R., Pierce, R. B., Nowlan, C. R., Abad, G. G., Nehrir, A. and Williams, D.: Evaluating Sentinel-5P TROPOMI tropospheric NO_2 column densities with airborne and Pandora spectrometers near New York City and Long Island Sound, Atmospheric Measurement Techniques, 13(11), 6113–6140, https://doi.org/10.5194/amt-13-6113-2020, 2020.

Jung, J., Souri, A. H., Wong, D. C., Lee, S., Jeon, W., Kim, J. and Choi, Y.: The Impact of the Direct Effect of Aerosols on Meteorology and Air Quality Using Aerosol Optical Depth Assimilation During the KORUS-AQ Campaign, Journal of Geophysical Research: Atmospheres, 124(14), 8303–8319, https://doi.org/10.1029/2019JD030641, 2019.

Jung, Y., González Abad, G., Nowlan, C. R., Chance, K., Liu, X., Torres, O., and Ahn, C.: Explicit Aerosol Correction of OMI Formaldehyde Retrievals, Earth and Space Science, 6, 2087–2105, https://doi.org/10.1029/2019EA000702, 2019.

Ke, Y., Leung, L. R., Huang, M., Coleman, A. M., Li, H. and Wigmosta, M. S.: Development of high resolution land surface parameters for the Community Land Model, Geoscientific Model Development, 5(6), 1341–1362, https://doi.org/10.5194/gmd-5-1341-2012, 2012.

Kleinman, L. I., Daum, P. H., Lee, Y.-N., Nunnermacker, L. J., Springston, S. R., Weinstein-Lloyd, J. and Rudolph, J.: Ozone production efficiency in an urban area, Journal of Geophysical Research: Atmospheres, 107(D23), ACH 23-1-ACH 23-12, https://doi.org/10.1029/2002JD002529, 2002.

Krotkov, N. A., McLinden, C. A., Li, C., Lamsal, L. N., Celarier, E. A., Marchenko, S. V., Swartz, W. H., Bucsela, E. J., Joiner, J., Duncan, B. N., Boersma, K. F., Veefkind, J. P., Levelt, P. F., Fioletov, V. E., Dickerson, R. R., He, H., Lu, Z. and Streets, D. G.: Aura OMI observations of regional SO_2 and NO_2 pollution changes from 2005 to 2015, Atmospheric Chemistry and Physics, 16(7), 4605–4629, https://doi.org/10.5194/acp-16-4605-2016, 2016.

Lamsal, L. N., Martin, R. V., Donkelaar, A. van, Steinbacher, M., Celarier, E. A., Bucsela, E., Dunlea, E. J. and Pinto, J. P.: Ground-level nitrogen dioxide concentrations inferred from the satellite-borne Ozone Monitoring Instrument, Journal of Geophysical Research: Atmospheres, 113(D16), https://doi.org/10.1029/2007JD009235, 2008.

Le Quéré, C., Jackson, R. B., Jones, M. W., Smith, A. J. P., Abernethy, S., Andrew, R. M., De-Gol, A. J., Willis, D. R., Shan, Y., Canadell, J. G., Friedlingstein, P., Creutzig, F. and

740   Peters, G. P.: Temporary reduction in daily global CO 2 emissions during the COVID-19
741   forced confinement, Nature Climate Change, 10(7), 647–653,
742   https://doi.org/10.1038/s41558-020-0797-x, 2020.
743 Le, T., Wang, Y., Liu, L., Yang, J., Yung, Y. L., Li, G. and Seinfeld, J. H.: Unexpected air
744   pollution with marked emission reductions during the COVID-19 outbreak in China,
745   Science, 369(6504), 702–706, https://doi.org/10.1126/science.abb7431, 2020.
746 Lee, J. D., Drysdale, W. S., Finch, D. P., Wilde, S. E. and Palmer, P. I.: UK surface NO_2 levels
747   dropped by 42 % during the COVID-19 lockdown: impact on surface O_3,
748   Atmospheric Chemistry and Physics, 20(24), 15743–15759, https://doi.org/10.5194/acp-
749   20-15743-2020, 2020.
750 Lelieveld, J., Berresheim, H., Borrmann, S., Crutzen, P. J., Dentener, F. J., Fischer, H., Feichter,
751   J., Flatau, P. J., Heland, J., Holzinger, R., Korrmann, R., Lawrence, M. G., Levin, Z.,
752   Markowicz, K. M., Mihalopoulos, N., Minikin, A., Ramanathan, V., Reus, M. de,
753   Roelofs, G. J., Scheeren, H. A., Sciare, J., Schlager, H., Schultz, M., Siegmund, P., Steil,
754   B., Stephanou, E. G., Stier, P., Traub, M., Warneke, C., Williams, J., and Ziereis, H.:
755   Global Air Pollution Crossroads over the Mediterranean, 298, 794–799,
756   https://doi.org/10.1126/science.1075457, 2002.
757 Levy, R. C., Mattoo, S., Munchak, L. A., Remer, L. A., Sayer, A. M., Patadia, F. and Hsu, N. C.:
758   The Collection 6 MODIS aerosol products over land and ocean, Atmospheric
759   Measurement Techniques, 6(11), 2989–3034, https://doi.org/10.5194/amt-6-2989-2013,
760   2013.
761 Li, K. and Lin, B.: Impacts of urbanization and industrialization on energy consumption/CO2
762   emissions: Does the level of development matter?, Renewable and Sustainable Energy
763   Reviews, 52, 1107–1122, https://doi.org/10.1016/j.rser.2015.07.185, 2015.
764 Lin, Y.-L., Farley, R. D. and Orville, H. D.: Bulk Parameterization of the Snow Field in a Cloud
765   Model, Journal of Applied Meteorology and Climatology, 22(6), 1065–1092,
766   https://doi.org/10.1175/1520-0450(1983)022<1065:BPOTSF>2.0.CO;2, 1983.
767 Liu, F., Page, A., Strode, S. A., Yoshida, Y., Choi, S., Zheng, B., Lamsal, L. N., Li, C., Krotkov,
768   N. A., Eskes, H., A, R. van der, Veefkind, P., Levelt, P. F., Hauser, O. P. and Joiner, J.:
769   Abrupt decline in tropospheric nitrogen dioxide over China after the outbreak of COVID-
770   19, Science Advances, 6(28), eabc2992, https://doi.org/10.1126/sciadv.abc2992, 2020.
771 Lorenz, E. N.: Deterministic Nonperiodic Flow, Journal of the Atmospheric Sciences, 20(2),
772   130–141, https://doi.org/10.1175/1520-0469(1963)020<0130:DNF>2.0.CO;2, 1963.
773 Marais, E. A., Jacob, D. J., Kurosu, T. P., Chance, K., Murphy, J. G., Reeves, C., Mills, G.,
774   Casadio, S., Millet, D. B., Barkley, M. P., Paulot, F. and Mao, J.: Isoprene emissions in
775   Africa inferred from OMI observations of formaldehyde columns, Atmospheric
776   Chemistry and Physics, 12(14), 6219–6235, https://doi.org/10.5194/acp-12-6219-2012,
777   2012.
778 Martin, R. V., Chance, K., Jacob, D. J., Kurosu, T. P., Spurr, R. J. D., Bucsela, E., Gleason, J. F.,
779   Palmer, P. I., Bey, I., Fiore, A. M., Li, Q., Yantosca, R. M., and Koelemeijer, R. B. A.:
780   An improved retrieval of tropospheric nitrogen dioxide from GOME, 107, ACH 9-1-
781   ACH 9-21, https://doi.org/10.1029/2001JD001027, 2002.
782 Miyazaki, K., Bowman, K., Sekiya, T., Jiang, Z., Chen, X., Eskes, H., Ru, M., Zhang, Y. and
783   Shindell, D.: Air Quality Response in China Linked to the 2019 Novel Coronavirus
784   (COVID-19) Lockdown, Geophysical Research Letters, 47(19), e2020GL089252,
785   https://doi.org/10.1029/2020GL089252, 2020.

786 Nevius, D. S. and Evans, C.: The Influence of Vertical Advection Discretization in the WRF-
787   ARW Model on Capping Inversion Representation in Warm-Season, Thunderstorm-
788   Supporting Environments, Weather and Forecasting, 33(6), 1639–1660,
789   https://doi.org/10.1175/WAF-D-18-0103.1, 2018.
790 Okruszek, Ł., Aniszewska-Stańczuk, A., Piejka, A., Wiśniewska, M., and Żurek, K.: Safe but
791   Lonely? Loneliness, Anxiety, and Depression Symptoms and COVID-19, Front.
792   Psychol., 11, https://doi.org/10.3389/fpsyg.2020.579181, 2020.
793 Ordóñez, C., Garrido-Perez, J. M. and García-Herrera, R.: Early spring near-surface ozone in
794   Europe during the COVID-19 shutdown: Meteorological effects outweigh emission
795   changes, Science of The Total Environment, 747, 141322,
796   https://doi.org/10.1016/j.scitotenv.2020.141322, 2020.
797 Parrish, D. D., Lamarque, J.-F., Naik, V., Horowitz, L., Shindell, D. T., Staehelin, J., Derwent,
798   R., Cooper, O. R., Tanimoto, H., Volz-Thomas, A., Gilge, S., Scheel, H.-E., Steinbacher,
799   M. and Fröhlich, M.: Long-term changes in lower tropospheric baseline ozone
800   concentrations: Comparing chemistry-climate models and observations at northern
801   midlatitudes, Journal of Geophysical Research: Atmospheres, 119(9), 5719–5736,
802   https://doi.org/10.1002/2013JD021435, 2014.
803 Pleim, J. E.: A Combined Local and Nonlocal Closure Model for the Atmospheric Boundary
804   Layer. Part I: Model Description and Testing, Journal of Applied Meteorology and
805   Climatology, 46(9), 1383–1395, https://doi.org/10.1175/JAM2539.1, 2007.
806 Pouyaei, A., Sadeghi, B., Choi, Y., Jung, J., Souri, A. H., Zhao, C., and Song, C. H.:
807   Development and Implementation of a Physics-Based Convective Mixing Scheme in the
808   Community Multiscale Air Quality Modeling Framework, 13, e2021MS002475,
809   https://doi.org/10.1029/2021MS002475, 2021.
810 Rodgers, C. D.: Inverse Methods for Atmospheric Sounding: Theory and Practice, WORLD
811   SCIENTIFIC, Oxford, 2000.
812 Rappenglück, B., Ackermann, L., Alvarez, S., Golovko, J., Buhr, M., Field, R. A., Soltis, J.,
813   Montague, D. C., Hauze, B., Adamson, S., Risch, D., Wilkerson, G., Bush, D.,
814   Stoeckenius, T., and Keslar, C.: Strong wintertime ozone events in the Upper Green
815   River basin, Wyoming, 14, 4909–4934, https://doi.org/10.5194/acp-14-4909-2014, 2014.
816 Salma, I., Vörösmarty, M., Gyöngyösi, A. Z., Thén, W. and Weidinger, T.: What can we learn
817   about urban air quality with regard to the first outbreak of the COVID-19 pandemic? A
818   case study from central Europe, Atmospheric Chemistry and Physics, 20(24), 15725–
819   15742, https://doi.org/10.5194/acp-20-15725-2020, 2020.
820 Seinfeld, J. H. and Pandis, S. N.: Atmospheric Chemistry and Physics: From Air Pollution to
821   Climate Change, 2nd edition., Wiley-Interscience, Hoboken, N.J., 2006.
822 Shi, X. and Brasseur, G. P.: The Response in Air Quality to the Reduction of Chinese Economic
823   Activities During the COVID-19 Outbreak, Geophysical Research Letters, 47(11),
824   e2020GL088070, https://doi.org/10.1029/2020GL088070, 2020.
825 Sicard, P., De Marco, A., Agathokleous, E., Feng, Z., Xu, X., Paoletti, E., Rodriguez, J. J. D. and
826   Calatayud, V.: Amplified ozone pollution in cities during the COVID-19 lockdown,
827   Science of The Total Environment, 735, 139542,
828   https://doi.org/10.1016/j.scitotenv.2020.139542, 2020.
829 Sillman, S.: The relation between ozone, NOx and hydrocarbons in urban and polluted rural
830   environments, Atmospheric Environment, 33(12), 1821–1845,
831   https://doi.org/10.1016/S1352-2310(98)00345-8, 1999.

Silvern, R. F., Jacob, D. J., Mickley, L. J., Sulprizio, M. P., Travis, K. R., Marais, E. A., Cohen, R. C., Laughner, J. L., Choi, S., Joiner, J. and Lamsal, L. N.: Using satellite observations of tropospheric NO_2 columns to infer long-term trends in US NO_x emissions: the importance of accounting for the free tropospheric NO_2 background, Atmospheric Chemistry and Physics, 19(13), 8863–8878, https://doi.org/10.5194/acp-19-8863-2019, 2019.

Skamarock, W. C. and Klemp, J. B.: A time-split nonhydrostatic atmospheric model for weather research and forecasting applications, Journal of Computational Physics, 227(7), 3465–3485, https://doi.org/10.1016/j.jcp.2007.01.037, 2008.

Souri, A. H., Nowlan, C. R., González Abad, G., Zhu, L., Blake, D. R., Fried, A., Weinheimer, A. J., Wisthaler, A., Woo, J.-H., Zhang, Q., Chan Miller, C. E., Liu, X. and Chance, K.: An inversion of NO_x and non-methane volatile organic compound (NMVOC) emissions using satellite observations during the KORUS-AQ campaign and implications for surface ozone over East Asia, Atmospheric Chemistry and Physics, 20(16), 9837–9854, https://doi.org/10.5194/acp-20-9837-2020, 2020a.

Souri, A. H., Nowlan, C. R., Wolfe, G. M., Lamsal, L. N., Chan Miller, C. E., Abad, G. G., Janz, S. J., Fried, A., Blake, D. R., Weinheimer, A. J., Diskin, G. S., Liu, X. and Chance, K.: Revisiting the effectiveness of HCHO/NO2 ratios for inferring ozone sensitivity to its precursors using high resolution airborne remote sensing observations in a high ozone episode during the KORUS-AQ campaign, Atmospheric Environment, 224, 117341, https://doi.org/10.1016/j.atmosenv.2020.117341, 2020b.

Souri, A. H., Choi, Y., Jeon, W., Kochanski, A. K., Diao, L., Mandel, J., Bhave, P. V., and Pan, S.: Quantifying the Impact of Biomass Burning Emissions on Major Inorganic Aerosols and Their Precursors in the U.S., 122, 12,020-12,041, https://doi.org/10.1002/2017JD026788, 2017.

Souri, Amir H., Chance, K., Bak, J., Nowlan, C., González Abad, G., Jung, Y., Wong, D., Mao, J., Liu, X.: COVID-19-Europe-Ozone-NOx-VOC, Mendeley Data, V1, doi: 10.17632/jchfxsrvsb.1, 2021

Souri, A. H., Chance, K., Sun, K., Liu, X., and Johnson, M. S.: Dealing with Spatial Heterogeneity in Pointwise to Gridded Data Comparisons, 1–33, Atmospheric Measurement Techniques Discussion, https://doi.org/10.5194/amt-2021-253, 2021.

Stavrakou, T., Müller, J.-F., Bauwens, M., De Smedt, I., Van Roozendael, M., Guenther, A., Wild, M. and Xia, X.: Isoprene emissions over Asia 1979–2012: impact of climate and land-use changes, Atmospheric Chemistry and Physics, 14(9), 4587–4605, https://doi.org/10.5194/acp-14-4587-2014, 2014.

Su, T., Li, Z. and Kahn, R.: Relationships between the planetary boundary layer height and surface pollutants derived from lidar observations over China: regional pattern and influencing factors, Atmospheric Chemistry and Physics, 18(21), 15921–15935, https://doi.org/10.5194/acp-18-15921-2018, 2018.

Sun, K., Li, L., Jagini, S., and Li, D.: A satellite-data-driven framework to rapidly quantify air-basin-scale NOx emissions and its application to the Po Valley during the COVID-19 pandemic, Atmospheric Chemistry and Physics, 21, 13311–13332, https://doi.org/10.5194/acp-21-13311-2021, 2021.

Thornton, J. A., Wooldridge, P. J., Cohen, R. C., Martinez, M., Harder, H., Brune, W. H., Williams, E. J., Roberts, J. M., Fehsenfeld, F. C., Hall, S. R., Shetter, R. E., Wert, B. P. and Fried, A.: Ozone production rates as a function of NOx abundances and HOx

878   production rates in the Nashville urban plume, Journal of Geophysical Research:
879   Atmospheres, 107(D12), ACH 7-1-ACH 7-17, https://doi.org/10.1029/2001JD000932,
880   2002.
881 United Nations Conference on Trade and Development Report, Accessed Dec 2020,
882   https://unctad.org/system/files/official-document/dtltlbinf2020d1_en.pdf
883 Valin, L. C., Fiore, A. M., Chance, K. and Abad, G. G.: The role of OH production in
884   interpreting the variability of CH2O columns in the southeast U.S., Journal of
885   Geophysical Research: Atmospheres, 121(1), 478–493,
886   https://doi.org/10.1002/2015JD024012, 2016.
887 Verhoelst, T., Compernolle, S., Pinardi, G., Lambert, J.-C., Eskes, H. J., Eichmann, K.-U.,
888   Fjæraa, A. M., Granville, J., Niemeijer, S., Cede, A., Tiefengraber, M., Hendrick, F.,
889   Pazmiño, A., Bais, A., Bazureau, A., Boersma, K. F., Bognar, K., Dehn, A., Donner, S.,
890   Elokhov, A., Gebetsberger, M., Goutail, F., Grutter de la Mora, M., Gruzdev, A., Gratsea,
891   M., Hansen, G. H., Irie, H., Jepsen, N., Kanaya, Y., Karagkiozidis, D., Kivi, R., Kreher,
892   K., Levelt, P. F., Liu, C., Müller, M., Navarro Comas, M., Piters, A. J. M., Pommereau,
893   J.-P., Portafaix, T., Prados-Roman, C., Puentedura, O., Querel, R., Remmers, J., Richter,
894   A., Rimmer, J., Rivera Cárdenas, C., Saavedra de Miguel, L., Sinyakov, V. P., Stremme,
895   W., Strong, K., Van Roozendael, M., Veefkind, J. P., Wagner, T., Wittrock, F., Yela
896   González, M. and Zehner, C.: Ground-based validation of the Copernicus Sentinel-5P
897   TROPOMI NO2 measurements with the NDACC ZSL-DOAS, MAX-DOAS and
898   Pandonia global networks, Atmospheric Measurement Techniques, 14(1), 481–510,
899   https://doi.org/10.5194/amt-14-481-2021, 2021.
900 Wang, P., Piters, A., van Geffen, J., Tuinder, O., Stammes, P. and Kinne, S.: Shipborne MAX-
901   DOAS measurements for validation of TROPOMI NO_2 products, Atmospheric
902   Measurement Techniques, 13(3), 1413–1426, https://doi.org/10.5194/amt-13-1413-2020,
903   2020.
904 Wang, W., Parrish, D. D., Li, X., Shao, M., Liu, Y., Mo, Z., Lu, S., Hu, M., Fang, X., Wu, Y.,
905   Zeng, L. and Zhang, Y.: Exploring the drivers of the increased ozone production in
906   Beijing in summertime during 2005–2016, Atmospheric Chemistry and Physics, 20(24),
907   15617–15633, https://doi.org/10.5194/acp-20-15617-2020, 2020.
908 Wolfe, G. M., Kaiser, J., Hanisco, T. F., Keutsch, F. N., de Gouw, J. A., Gilman, J. B., Graus,
909   M., Hatch, C. D., Holloway, J., Horowitz, L. W., Lee, B. H., Lerner, B. M., Lopez-
910   Hilifiker, F., Mao, J., Marvin, M. R., Peischl, J., Pollack, I. B., Roberts, J. M., Ryerson,
911   T. B., Thornton, J. A., Veres, P. R. and Warneke, C.: Formaldehyde production from
912   isoprene oxidation across NO_x regimes, Atmospheric Chemistry and Physics, 16(4),
913   2597–2610, https://doi.org/10.5194/acp-16-2597-2016, 2016.
914 Wyche, K. P., Nichols, M., Parfitt, H., Beckett, P., Gregg, D. J., Smallbone, K. L. and Monks, P.
915   S.: Changes in ambient air quality and atmospheric composition and reactivity in the
916   South East of the UK as a result of the COVID-19 lockdown, Science of The Total
917   Environment, 755, 142526, https://doi.org/10.1016/j.scitotenv.2020.142526, 2021.
918 Xiu, A. and Pleim, J. E.: Development of a Land Surface Model. Part I: Application in a
919   Mesoscale Meteorological Model, Journal of Applied Meteorology and Climatology,
920   40(2), 192–209, https://doi.org/10.1175/1520-
921   0450(2001)040<0192:DOALSM>2.0.CO;2, 2001.

Yienger, J. J. and Levy, H.: Empirical model of global soil-biogenic NOx emissions, Journal of
Geophysical Research, 100(D6), 11447–11464, https://doi.org/10.1029/95JD00370,
1995.

Zhao, X., Griffin, D., Fioletov, V., McLinden, C., Cede, A., Tiefengraber, M., Müller, M.,
Bognar, K., Strong, K., Boersma, F., Eskes, H., Davies, J., Ogyu, A. and Lee, S. C.:
Assessment of the quality of TROPOMI high-spatial-resolution NO_2 data products in the
Greater Toronto Area, Atmospheric Measurement Techniques, 13(4), 2131–2159,
https://doi.org/10.5194/amt-13-2131-2020, 2020.

939
940
941 **Table 1.** Statistics reported in several validations studies comparing TROPOMI
942 tropospheric NO$_2$ against independent observations.
943

Study	Location	Time Period	Benchmark Instrument	Bias (low)	Dispersion	Modification	Modified Bias (low)
Chan et al. 2020	Munich	May 2018-Apr 2019	MAX-DOAS	30%	N/A	In-situ MAX-DOAS profiles	17%
Griffin et al. 2019	Canadian Oil Sands	Mar-May 2018 (v1.01)	Pandora (direct Sun)	15-30%	N/A	Higher resolution profiles (10 km) and albedo	0-25%
Judd et al. 2020	New York	Jun-Sep 2018	GeoTASO	19-33%	N/A	Higher resolution profiles (12 km)	7-19%
Verhoelst et al. 2020	Global	Apr 2018-Feb 2020	MAX-DOAS	37% (average), 23-51% (range)	3.5×10^{15} molec/cm^2	N/A	N/A
Wang P. et al. 2020	Atlantic and Pacific Oceans	4 campaigns during Dec 2018-Jul 2019	MAX-DOAS	Negligible	N/A	N/A	N/A
Zhao et al. 2020	Greater Toronto Area	Mar 2018-Mar 2019	Pandora (direct Sun)	24-28% (suburban/urban) +4-10% (rural)		Higher resolution profiles (10 km) and albedo	13-24% (suburban/urban) +14-15% (rural)

944
945
946

947

948

949
950
951
952 **Table 2.** Reaction rates relating to the chemical pathways of ozone formation and loss over box L
953 (proximity of central Europe).

Reactions	Production (P) or loss (L)	April 2020 (ppbv/hr)	April 2019 (ppbv/hr)	Net diff [a](ppbv/hr)
HO_2+NO	P	0.85	0.91	-0.06
RO_2+NO	P	0.44	0.41	+0.03
NO_2+OH	L	0.10	0.14	+0.04
O^1D+H_2O	L	0.07	0.08	+0.01
O_3+VOCs	L	0.01	0.01	0.00
O_3+HO_x	L	0.09	0.08	-0.01
$J_{NO2}[NO_2]$	P	14.61	27.28	-12.67
$k_{NO+O3}[NO][O_3]$	L	15.11	28.52	+13.40
$J_{NO2}[NO_2]- k_{NO+O3}[NO][O_3]$	N/A	-0.50	-1.24	+0.74
Numerically solved PO_3	N/A	-0.79	-1.53	+0.74

954 [a] A positive net difference indicates higher (lower) production (loss) in 2020 with respect to 2019.
955

956

CMAQ 15-km Domain

957
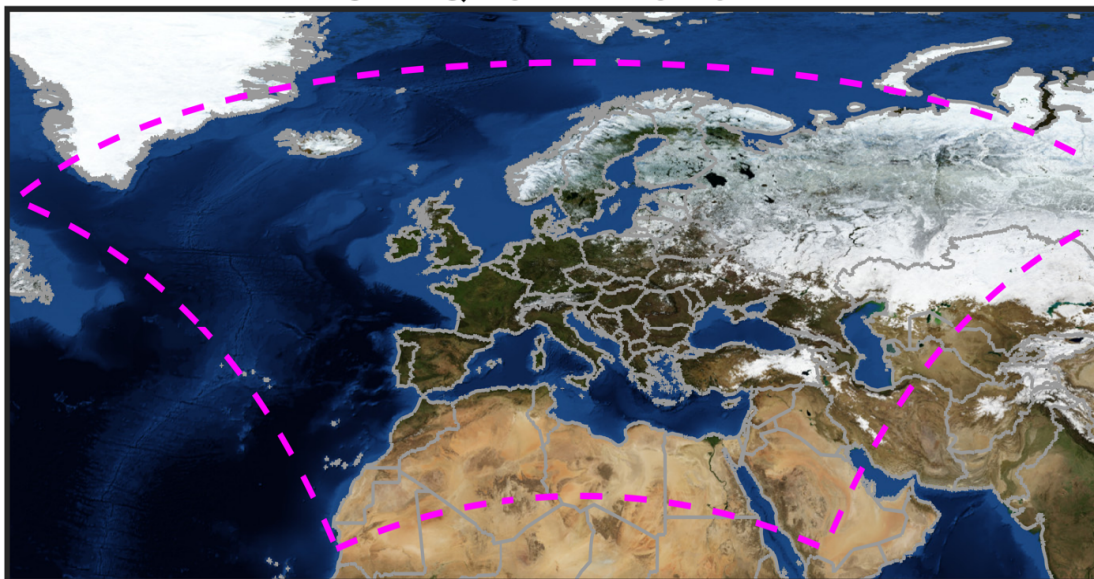
958   **Figure 1.** The WRF-CMAQ 15 km domain covering Europe. The background picture is based
959   on the publicly available NASA Blue Marble (© NASA).
960

961
962
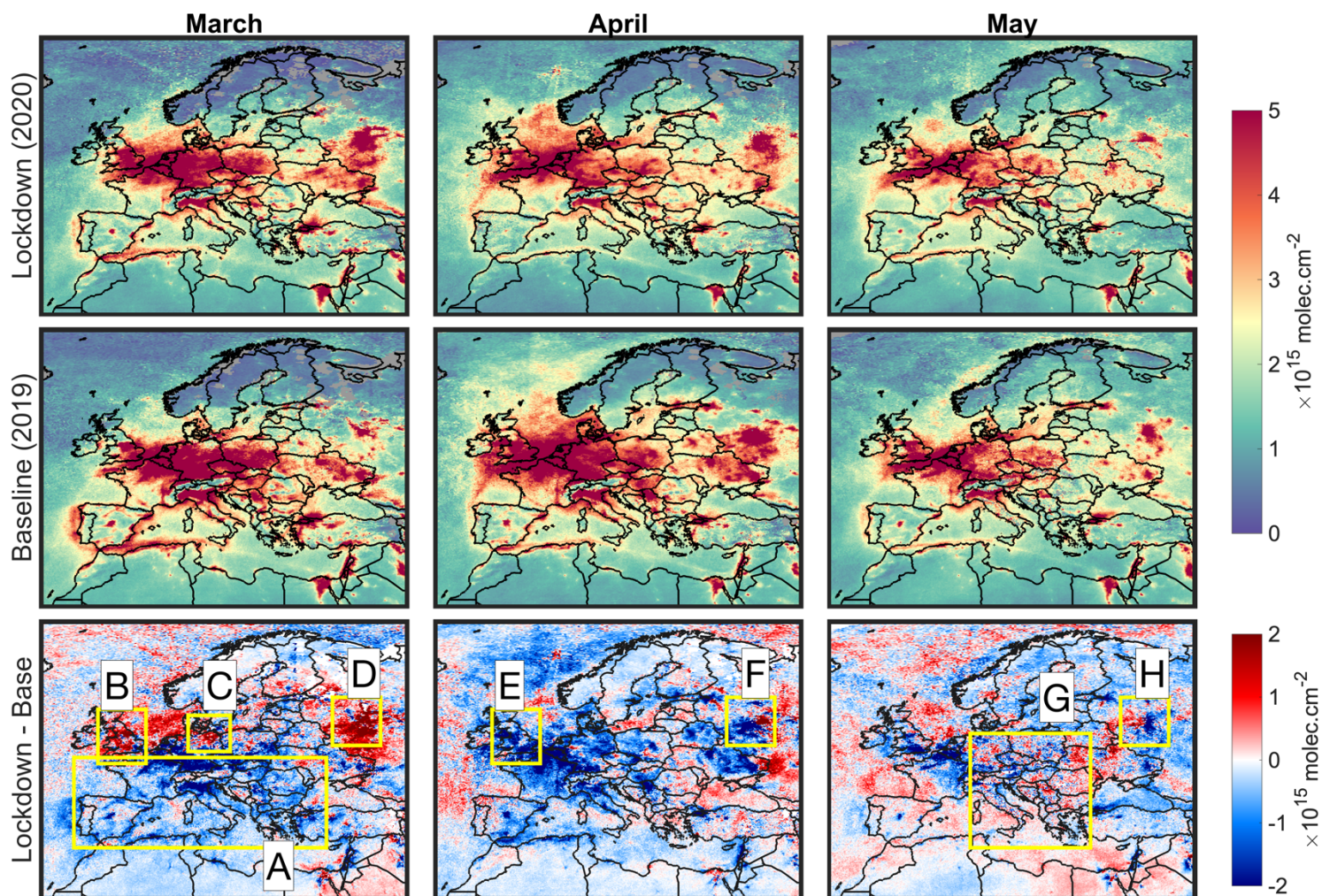
Figure 2. (first row) Maps of tropospheric NO$_2$ from the TROPOMI sensor during months of March, April, and May in 2020 (lockdown). (second row) Same as the first row but for the baseline year (2019). (last row), Difference of the columns in 2020 with respect to those of 2019. All columns are corrected for the bias and their AMFs are recalculated iteratively based on the posterior profiles derived from our inverse modeling practice. The satellite-derived columns are subject to errors, so a direct interpretation of their magnitudes cannot be performed in a robust manner.

971

972

973
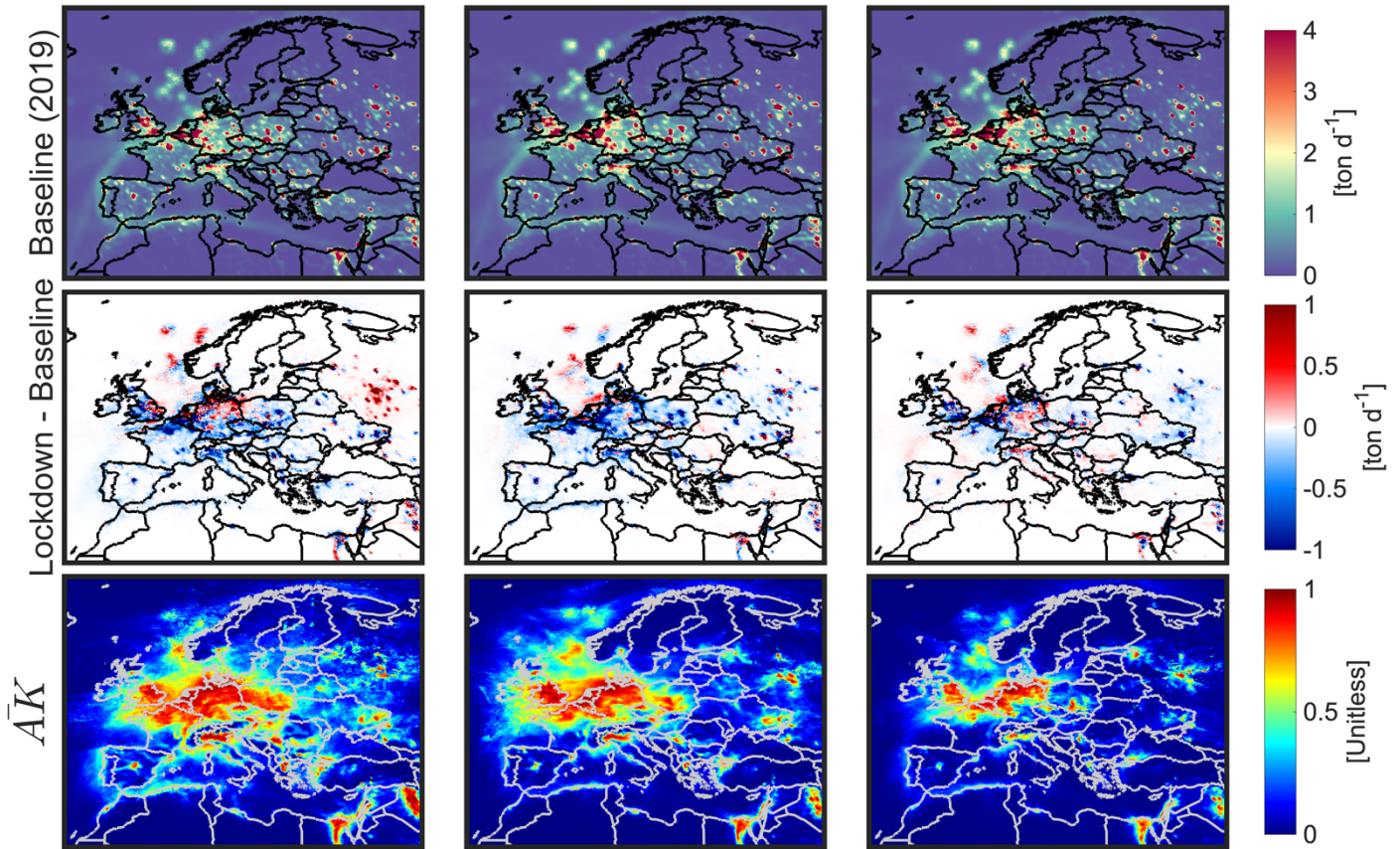
975 **Figure 3.** Top-down estimates of total NO$_x$ during months of March, April and May in 2019
976 (baseline) and the differences between emission in 2020 (lockdown) and 2019. To infer the
977 magnitude of emissions in 2020, the second row should be added to the first one. Both TROPOMI
978 HCHO and NO$_2$ observations are jointly used to estimate these numbers. Averaging kernels (mean
979 values based on both 2019 and 2020 estimates) describe the level of credibility of the estimate which
980 is heavily dependent on the TROPOMI signal-to-noise ratios.

981

982

983

984

985

986
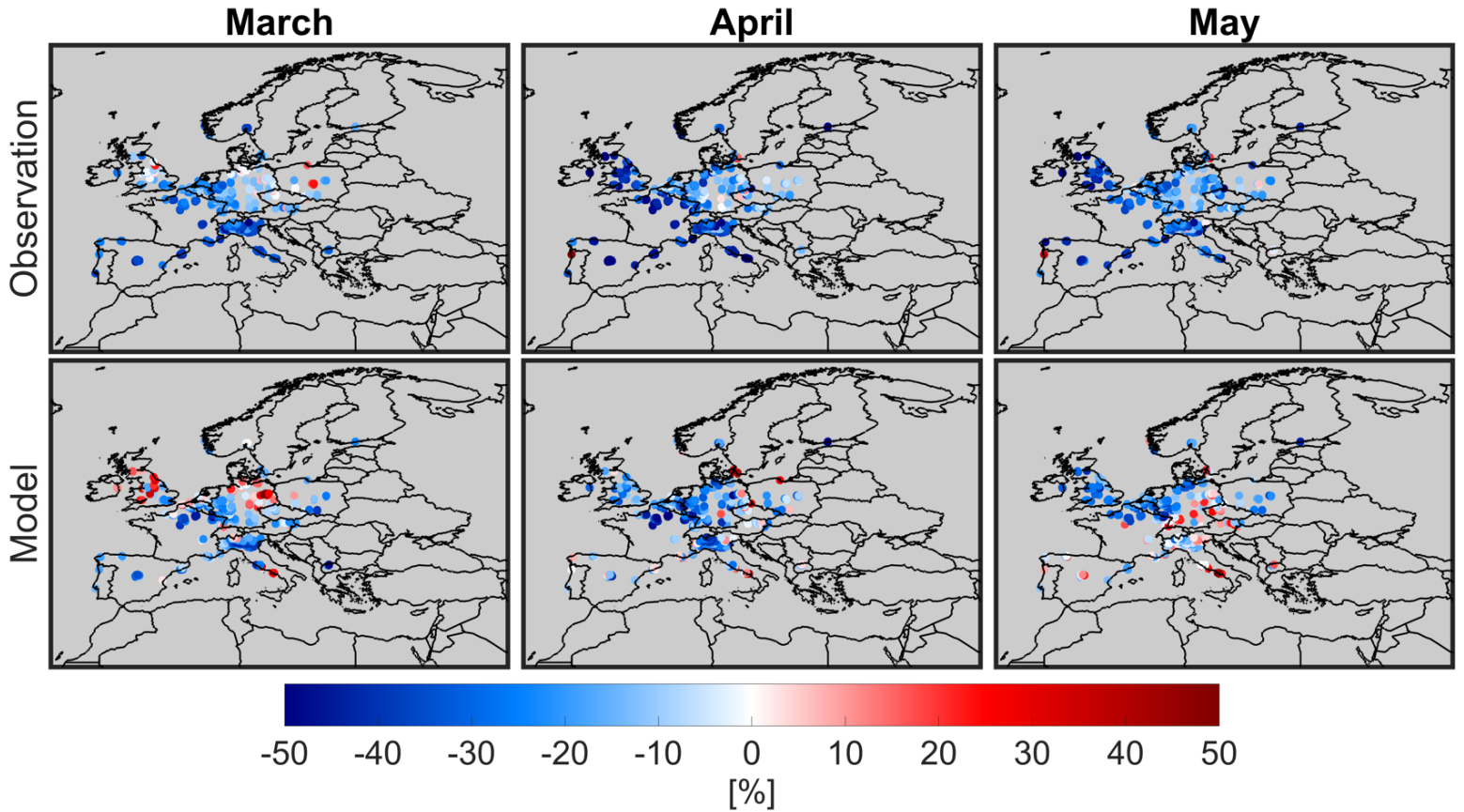
988   **Figure 4.** Scatter maps of relative changes in surface NO_2 concentrations suggested by the

989   European air quality network (first row), and the constrained model (second row). Results are

990   daily-averaged. We only consider grid cells whose averaging kernels (from the NO_x inversion)

991   are above 0.5. Furthermore, grid cells having more than 2 stations are only included to partly

992   account for the spatial representivity factor. Surface concentrations are not accounted for the

993   NO_z family interferences.

994
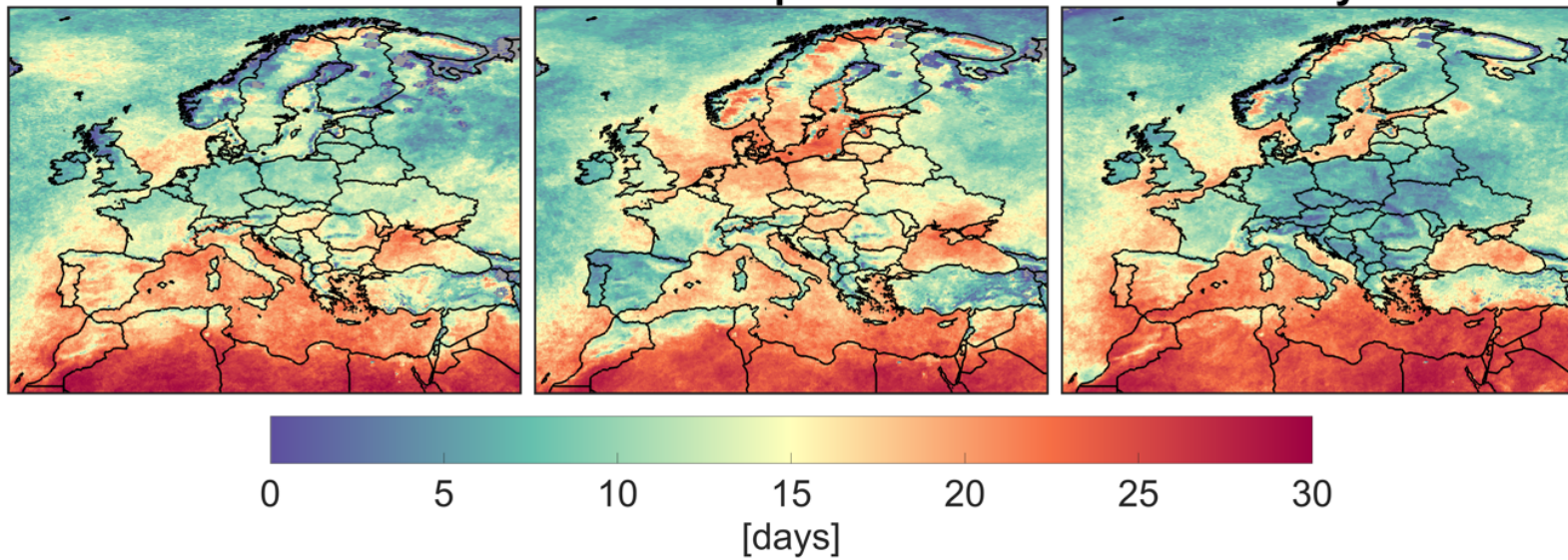
Figure 5. The average number of good quality (qa_flag>0.75) TROPOMI tropospheric NO_2 days observed at 15×15 km^2 in 2019 and 2020. These numbers are heavily affected by cloudiness.

1001

1002
1003
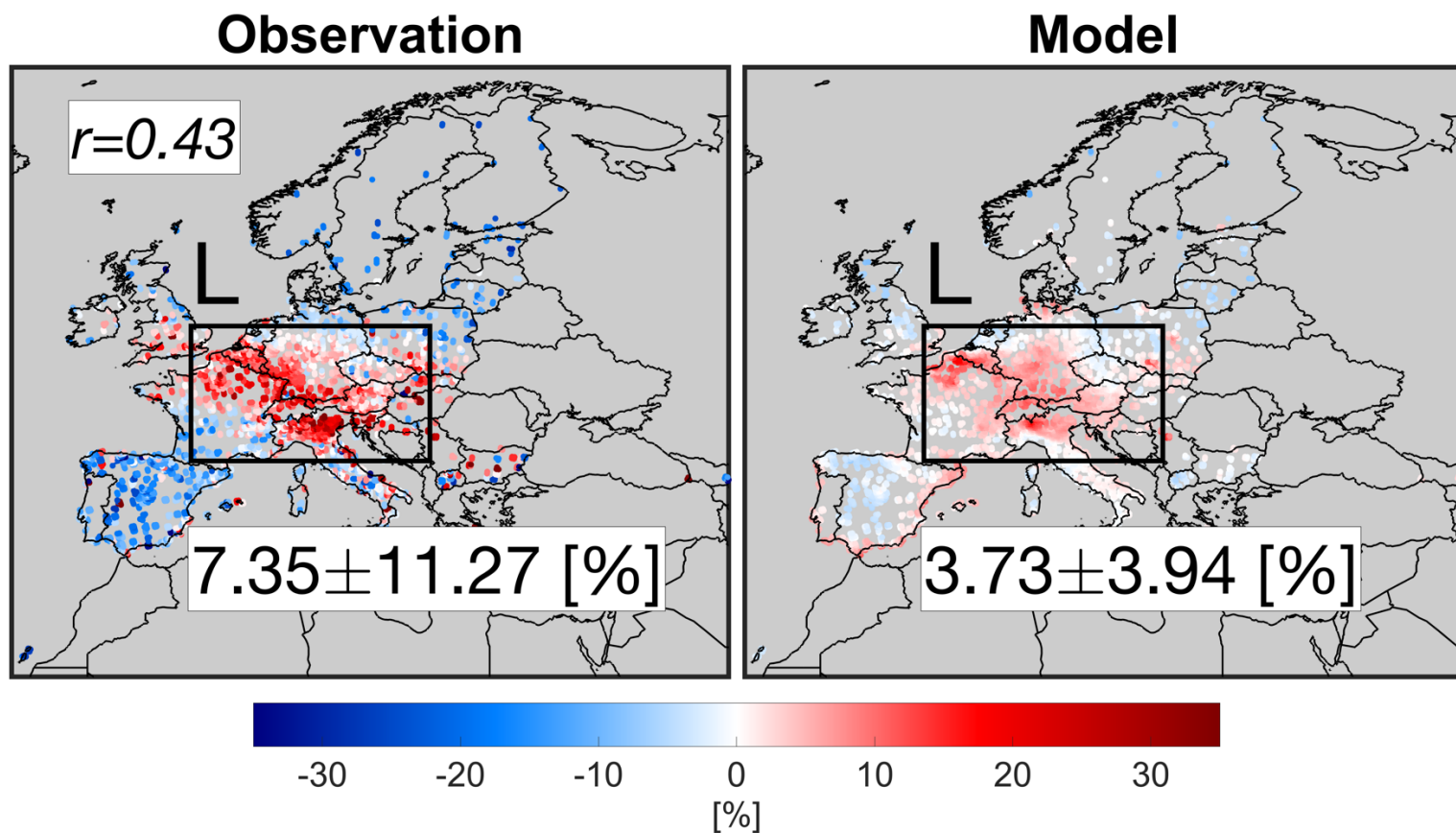
1005   **Figure 6.** Changes in surface MDA8 ozone concentrations suggested by the observation (left),

1006   and the constrained model (right) in April 2020 relative to those in 2019. The numbers are based

1007   on the box L region.

1008
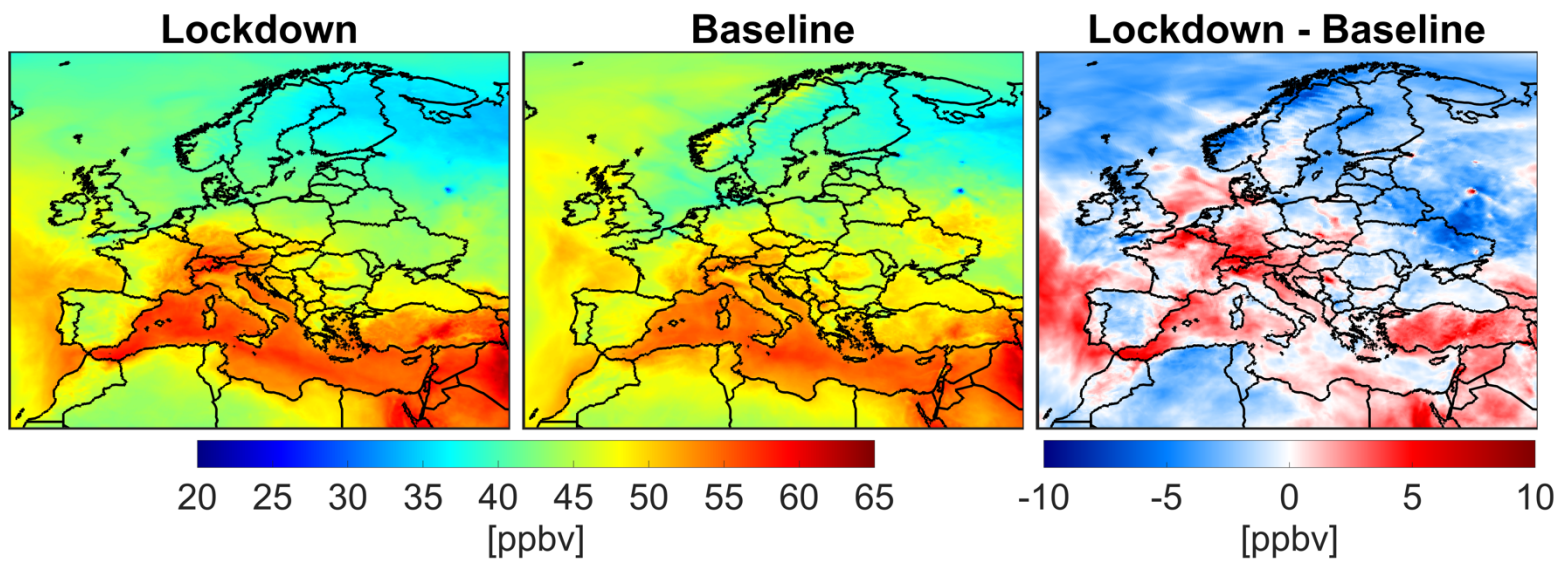
1010   **Figure 7.** Simulated surface MDA8 ozone concentration using the constrained model in the month

1011   of April 2020 (lockdown), April 2019 (baseline), and their difference.

1012

1013

1014
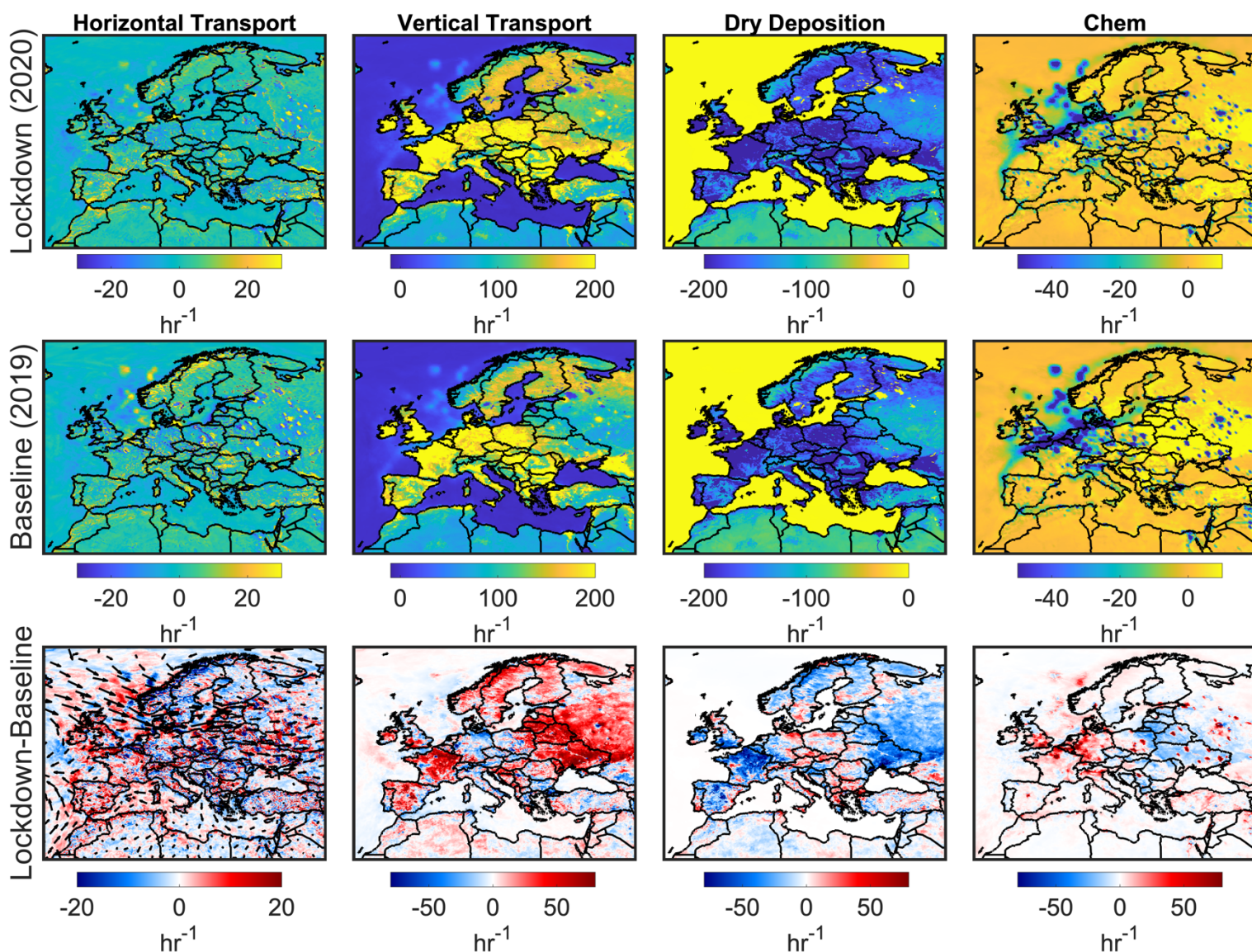
1016   **Figure 8.** Surface process tendencies (hr^{-1}) including horizontal transport (advection plus

1017   diffusion), vertical transport (advection plus diffusion), dry deposition, and chemistry. Positive

1018   (negative) values mean source (sink) of ozone. These outputs are based on the constrained

1019   model. Wind vectors are the difference.

1020

1021

1022
1023
1024
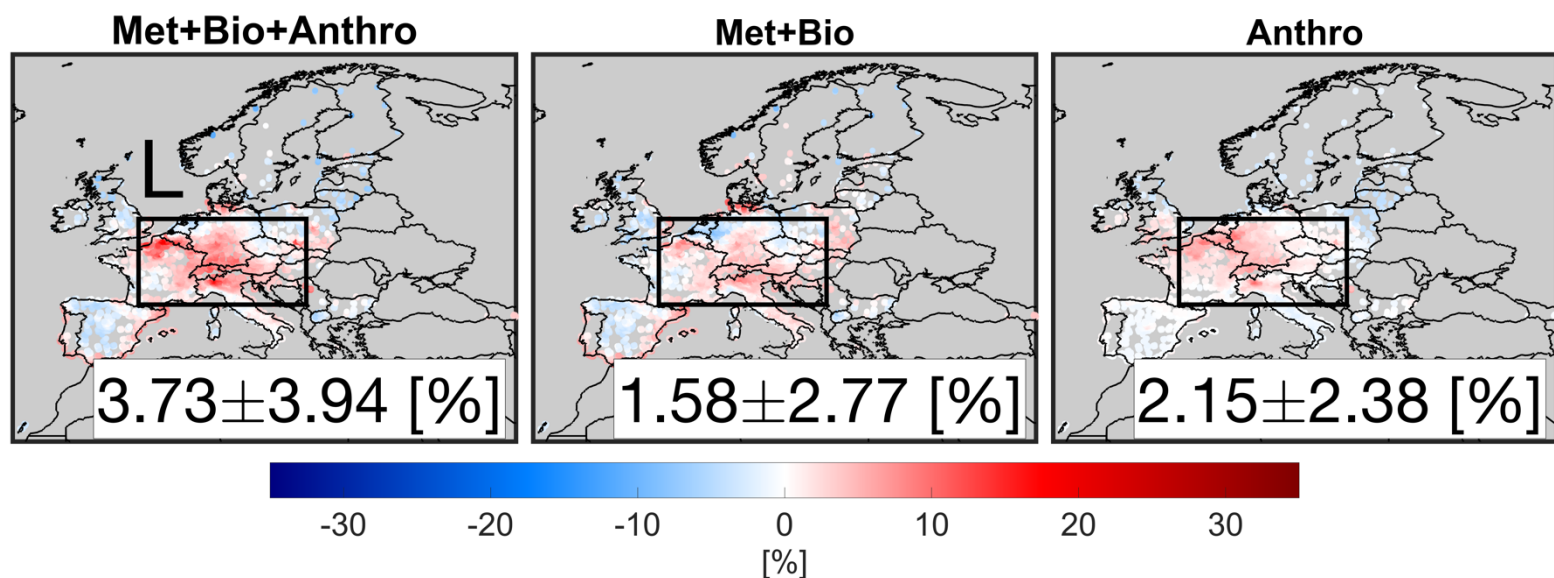
1026 **Figure 9.** Simulated MDA8 surface ozone difference between April 2020 with respect to April

1027 2019 including (left) dynamical meteorology, biogenic and anthropogenic emissions, (middle)

1028 dynamical meteorology and biogenic emissions, and (right) the subtraction of the previous

1029 scenarios isolating dynamical anthropogenic emissions. Emissions used for these experiments

1030 are based on the top-down estimates.

1031
1032

1033

1034
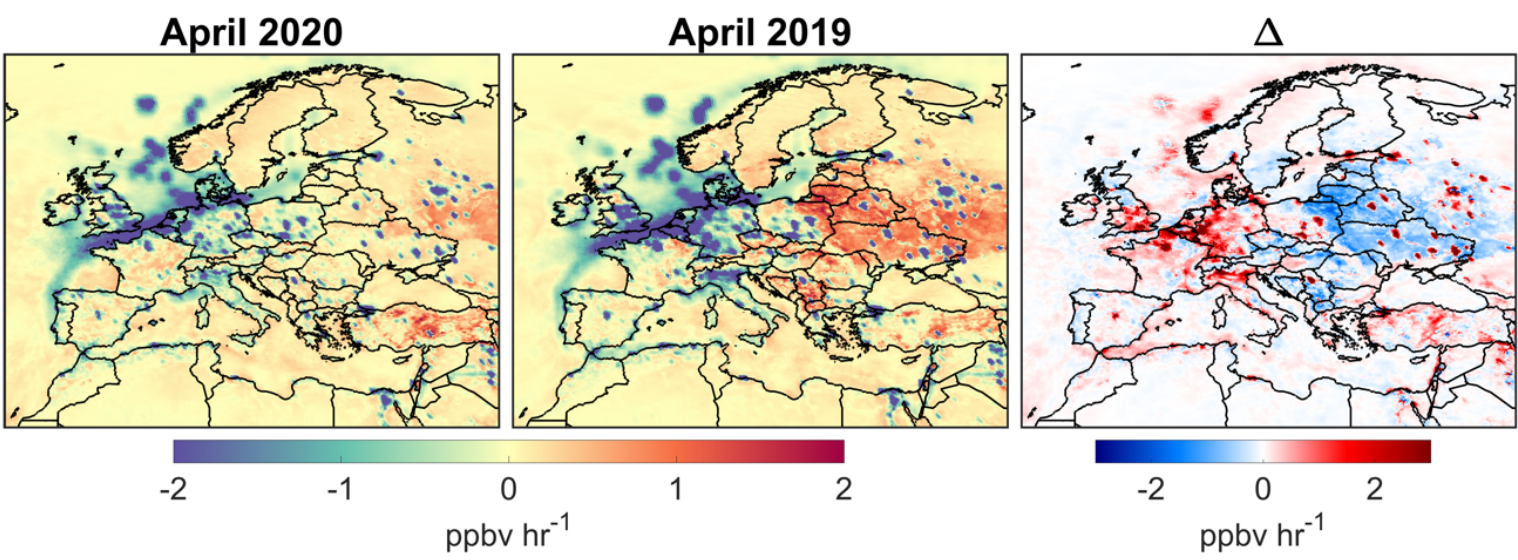
1036 **Figure 10.** Numerically-solved net ozone production rates based on the WRF-CMAQ simulations

1037 using the constrained emissions by the satellite data in April 2020, 2019, and the difference. These

1038 values are over the surface and are averaged during the MDA8 hours.

1039
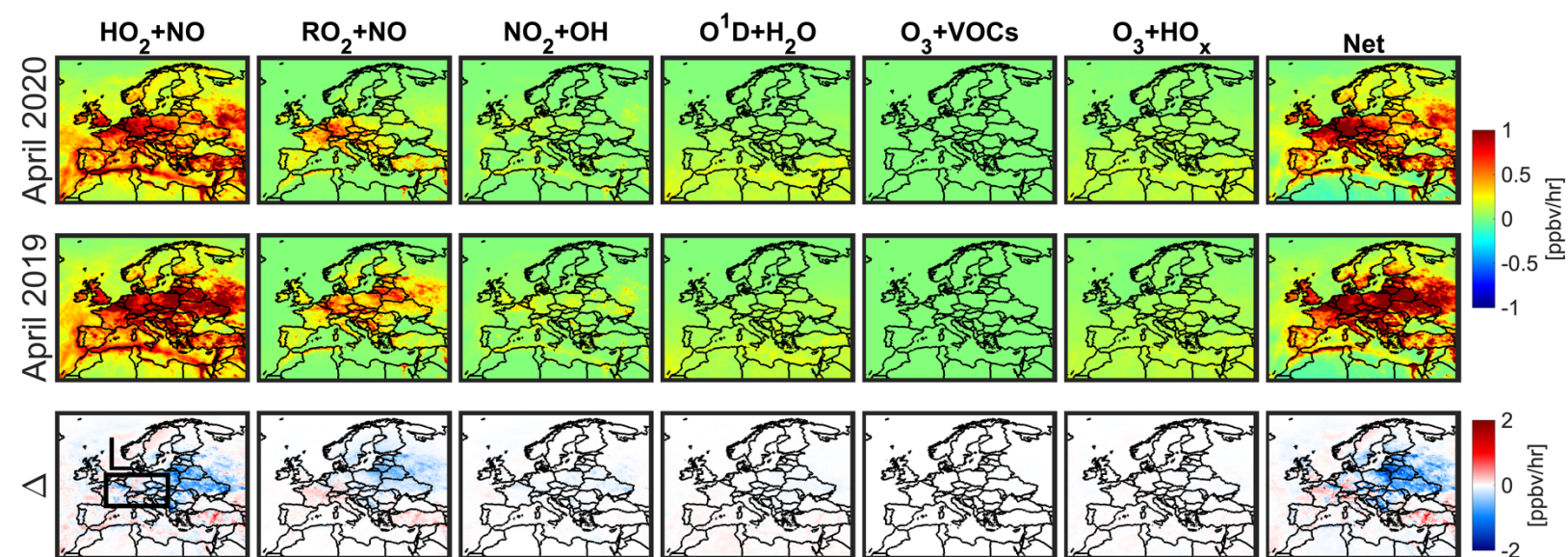
1041 **Figure 11.** Surface chemical processes involved in equation 5 (ppbv hr^{-1}) pertaining to the

1042 production and loss of ozone in April 2020 (lockdown) and 2019 (baseline) during MDA8 hours.

1043 These outputs are based on the constrained model.

1044
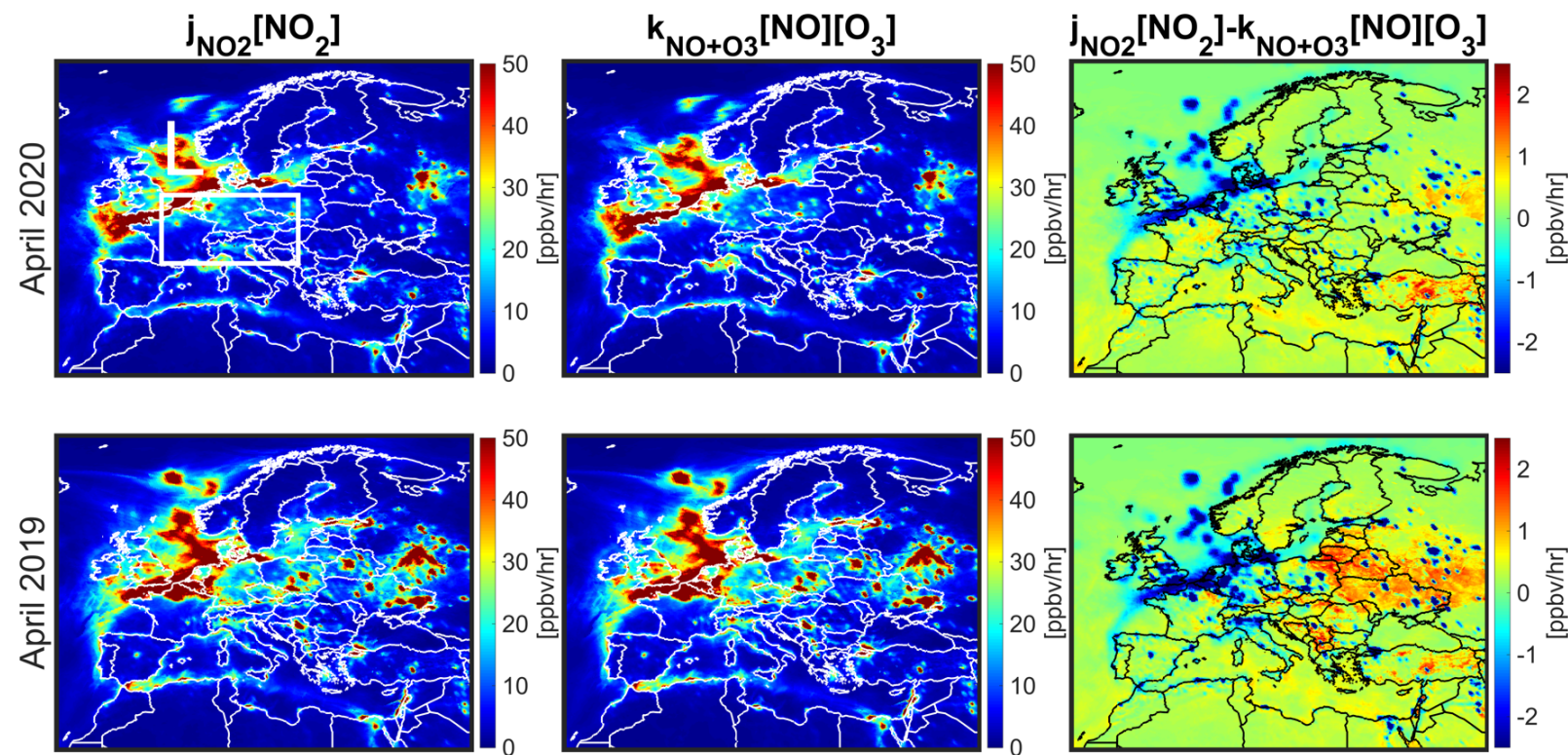
1046 **Figure 12.** Surface chemical processes involved in equation 6 (ppbv hr^{-1}) pertaining to the O$_3$-

1047 NO-NO$_2$ partitioning in April 2020 and 2019 during MDA8 hours. The constrained model by the

1048 satellite observations is used to derive these outputs.

1049

1050

1051